

Evaluating the temporal capability of empirical climatologies for rapid long-range volcanic infrasound propagation estimates using a multi-decadal dataset of persistent Vanuatu volcanic eruptions

Rodrigo De Negri¹, Robin S. Matoza¹, Patrick Hupe², Alexis Le Pichon³, Kaelynn M. Rose¹, S. Cevuard⁴, and J. J. Niroa⁴

¹ Department of Earth Science and Earth Research Institute, University of California, Santa Barbara, Santa Barbara, CA, USA

² BGR, B4.3, Hannover, Germany

³ CEA, CEA/DAM/DIF, F-91297 Arpajon, France

⁴ Vanuatu Meteorology and Geo-Hazards Department, PMB 9054, Lini Highway, Port Vila, Vanuatu

16 January 2025

SUMMARY

Powerful infrasound (acoustic waves <20 Hz) can be produced by explosive volcanic eruptions. The long-range propagation capability, over hundreds to thousands of kilometers, of atmospheric infrasound motivates the development of regional or even global scale volcano-infrasound monitoring systems. Infrasound propagation paths are subject to spatiotemporal atmospheric dynamics, which lead to deviations in the direction-of-arrival (back-azimuth) observed at sensor arrays and contribute to source location uncertainty. Here we further investigate the utility of empirical climatologies combined with 3-dimensional ray-tracing for providing first-order estimates of infrasound propagation paths and back-azimuth deviation corrections. The intended application is in scenarios requiring rapid or precomputed infrasound propagation calculations, such as for a volcano-infrasound monitoring system. Empirical climatologies are global observationally based function fitting models of the atmosphere, representing robust predictors of the bulk diurnal to seasonal atmospheric variability. Infrasound propagation characteristics have previously been shown to have strong seasonal and diurnal components. At the International Monitoring System (IMS) infrasound station IS22, New Caledonia, quasi-continuous multi-year infrasound array detections show oscillating azimuthal variations for arrivals from volcanoes in Vanuatu, including Yasur (~ 400 km range), Ambrym (~ 670 km range), and Lopevi (~ 650 km range). We perform 3-dimensional ray-tracing to model infrasound propagation from the Ambrym and Yasur volcano locations to IS22 every six hours (00:00, 06:00, 12:00, and 18:00 UTC) for every day of 2004 and 2019 for Ambrym and Yasur, respectively and evaluate the results as compared to the multi-year observations. We assess a variety of models and parameterizations, including both empirical climatologies and hybrid descriptions; range-independent and range dependent atmospheric discretizations; and unperturbed and perturbed range-independent empirical climatologies. The hybrid atmospheric descriptions are composed of ERA 5 reanalysis descriptions from the European Centre for Medium-Range Weather Forecasts (ECMWF) below ~ 80 km altitude combined with empirical climatologies above. We propose and employ simple parametric perturbations to the empirical climatologies, which are designed to enhance the stratospheric duct and compensate for missing gravity wave perturbations not included in the climatologies, and thereby better match observations. We build year-long back-azimuth deviation interpolations from the simulations and compare them with three different multi-year array detection datasets from IS22 covering from 2003 up to 2022. Through a systematic comparison, we find that the range-independent empirical climatologies can capture bulk azimuth deviation variability and could thus be useful for rapid infrasound propagation calculation scenarios, particularly during favorable sustained propagation ducting conditions. We show that the hybrid models better describe infrasound propagation during periods of weak stratospheric ducting and during transient atmospheric changes such as stratospheric wind reversals. Overall, our results support the notion that climatologies, if perturbed to compensate for missing gravity wave structure, can improve rapid low-latency and precomputed infrasound source discrimination and location procedures.

Key words: Infrasound, Volcano/climate interactions, Remote sensing of volcanoes, Volcano monitoring, Atmospheric effects (volcano), Numerical modelling

1 INTRODUCTION

Explosive volcanic eruptions are formidable sources of infrasound (acoustic waves <20 Hz), perhaps even the most powerful kind of infrasound recorded on Earth (Matoza et al. 2022b; Vergoz et al. 2022). Infrasound from a typical VEI 4 eruption (e.g., Matoza et al. 2011a, 2018) can propagate hundreds to thousands of kilometers due to low intrinsic attenuation (Sutherland & Bass 2004) and the formation of atmospheric ducts. These waveguides result from the combination of vertical gradients in horizontal winds and temperature, primarily at stratospheric and thermospheric altitudes (e.g., Dabrowa et al. 2011; Le Pichon et al. 2009b; Matoza et al. 2011a, 2018, 2019, 2022b; Vergoz et al. 2022; Waxler & Assink 2019).

The International Monitoring System (IMS) of the Comprehensive Nuclear-Test-Ban Treaty Organization (CTBTO) includes a global infrasound network that currently has 53 certified of 60 planned infrasound arrays (Christie & Campus 2010; Marty 2019). The IMS, designed to detect explosions with a yield greater than 1 kT TNT equivalent anywhere on Earth (Green & Bowers 2010; Le Pichon et al. 2009a; Marty 2019), has recorded numerous eruptions (Campus & Christie 2009; Matoza et al. 2019; Dabrowa et al. 2011). For example, 68 of 110 volcanic events worldwide ($\sim 61\%$) were detected by at least one infrasound station from 2002 to 2009 (Dabrowa et al. 2011), while up to 41 IMS stations were recording (Hedlin et al. 2002; Christie & Campus 2010; Hupe et al. 2022).

Previous studies have shown that we can use several infrasound arrays to detect, locate, and track the chronology of distant volcanic eruptions, and provide eruption source parameters for ash transport and dispersal models (e.g., Caudron et al. 2015; Dabrowa et al. 2011; Fee et al. 2010; Garcés et al. 2008; Green et al. 2013; Marchetti et al. 2013; Matoza et al. 2007, 2018, 2011a,b, 2017; Perttu et al. 2020; Taisne et al. 2019). Although most practical algorithms require detection by at least two or three infrasound arrays (stations) to locate the source (e.g., Arrowsmith et al. 2008; Evers & Haak 2005; Matoza et al. 2017, 2011a; Modrak et al. 2010; Morton & Arrowsmith 2014), single-station detection (i.e., detection by one array) of volcanic infrasound signals can still provide valuable information on eruption occurrence (e.g., De Angelis et al. 2012; De Negri et al. 2022; Fee et al. 2010; Gheri et al. 2023; Marchetti et al. 2019; Matoza et al. 2019; Morelli et al. 2022; Ortiz et al. 2020). Long-range infrasound also provides observational constraints on the activity of very remote volcanoes, such as those in the South Sandwich Islands, that can be challenging to observe with satellite remote sensing and for which local instrumentation is difficult to maintain (De Negri et al. 2022).

The dynamic nature of the atmosphere presents a major challenge for infrasound monitoring. Spatiotemporal variability at temporal scales including hourly, daily, and seasonal, and at spatial scales from the microscale to synoptic scale, is partially captured by various different atmospheric specification products (Drob et al. 2010; Schwaiger et al. 2019; Garcés et al. 1998; Smets et al. 2016). One of the most important atmospheric phenomena influencing infrasound propagation are the vector wind fields, which can create infrasound waveguides (along-path winds), but also impose cross-path winds (cross-winds) leading to deviations from the great-circle path connecting the true source and receiver locations (back-azimuth deviations), and upwinds resulting in shadow zones (e.g., Evers & Haak 2005; Matoza et al. 2011a; Green et al. 2012; De Negri & Matoza 2023). The back-azimuth deviations can be up to $\sim 10^\circ$ (e.g. Le Pichon et al. 2005c; Antier et al. 2007; Assink et al. 2014a; Morelli et al. 2022), resulting in source mislocations of up to hundreds of kilometers at remote distances (>250 km) if

using cross-bearing (i.e., triangulation) methods (De Negri & Matoza 2023; Matoza et al. 2017, 2018, 2011b).

Morton & Arrowsmith (2014) showed that by combining 3D ray-tracing techniques with realistic atmospheric profiles, lookup tables for celerity (ratio of range over total travel-time) and back-azimuth priors can be produced to describe global seasonal effects that could improve infrasound detection, location and association. A similar approach was used by Drob et al. (2010), who proposed combining the τ - p equations (Garcés et al. 1998) and hybrid ground-to-space (G2S) atmospheric descriptions of Drob et al. (2003), to account for hourly, daily, and seasonal changes for real time detection, location, and characterization automated algorithms at the International Data Center (IDC) of the CTBTO.

Building on the previous ideas, Matoza et al. (2018) and De Negri & Matoza (2023) showed that the mislocation of known volcanic sources could be reduced by an order of magnitude by applying corrections to observed back-azimuths before locating the source with a brute-force, grid-search, cross-bearings method (Matoza et al. 2017). De Negri & Matoza (2023) compared the results of using different atmospheric models in this approach, and found that statistical models, also known as empirical climatologies (i.e., the Horizontal Wind Model HWM14 (Drob et al. 2015) and the MSIS2.0 model (Emmert et al. 2020)), can be used to generate back-azimuth corrections that perform comparably well to those calculated using the more advanced and accurate hybrid models (e.g., the European Centre for Medium-Range Weather Forecasts (ECMWF) reanalysis v5 (ERA5) for the first ~ 80 km of the atmosphere merged with the empirical climatologies for higher altitudes). However, their study was limited to two eruption case studies lasting only several days, a small time window embedded in much larger temporal changes.

It is clear that, in terms of temporal and spatial accuracy, the best available descriptors of the lower atmosphere (<80 km) are the Numerical Weather Prediction (NWP) models (e.g., ECMWF). This is the main reason why the use of empirical climatologies is usually overlooked for infrasound propagation. However, there is an unavoidable trade-off between accuracy and computation resources that scales substantially with the model size. Thus, we usually need to choose either a static atmosphere for a large model or a small model with better accuracy but much more demanding calculations (and a good internet connection). We argue that there is a middle ground where the empirical climatologies and spherical range-independent ray-tracing can play a crucial role for first-order global characterization of infrasound propagation that has not been exploited for volcanic near-real time location and characterization. At present, global infrasound propagation results remain accessible only as reference summaries and there are no easy operational tables that could be directly implemented at volcanic observatories (e.g., lookup tables). Additionally, infrasound propagation can involve the thermosphere, which is not included in current NWP products, and a hybrid model fusing the NWP in the lower atmosphere with an empirical climatology for the upper atmosphere is required, but at greater computational complexity (Drob et al. 2003; Schwaiger et al. 2019). Infrasound arrivals that refract back to the surface from thermospheric heights (~ 110 km) have been observed (e.g., De Negri et al. 2022; Le Pichon et al. 2005b; Green et al. 2011) and are commonly modeled with ray-tracing techniques. The empirical climatologies map altitudes up to the exobase (~ 600 km), allowing thermospheric returns to be simulated within the propagation models.

The methodology introduced by De Negri & Matoza (2023) uses readily accessible numerical tools and offer a reproducible

workflow for calculation of lookup back-azimuth tables for arbitrary source-receiver locations, considering infrasound arrivals up to thermospheric altitudes. The rapid, first-order approach also reduces the computation burden that more accurate models require. Here, we evaluate the accuracy of their methodology with observations from the IMS infrasound array IS22, New Caledonia, which has recorded persistent infrasound from volcanoes in the Vanuatu volcanic archipelago (~400 to 700 km) during the last 20 years (2003–2022) (e.g., Antier et al. 2007; Assink et al. 2014a; Le Pichon et al. 2005a, 2006; Morelli et al. 2022). We calculate year-long infrasound back-azimuth estimates for arrivals at IS22 using both empirical and hybrid atmospheric specifications, and compare these results to the directions of Yasur and Ambrym volcanoes, which have exhibited persistent activity over the past 20 years of IS22 recording. We show that for long-range propagation models with year-long time scales, the simpler, first-order approach based on the empirical climatologies and range-independent (spherically layered) atmosphere provides comparable results with the hybrid models that use ECMWF specifications for the lower atmosphere. As such, the calculated lookup tables can be robust descriptors of seasonal changes and provide useful information for global monitoring and characterization of infrasound sources. Operationally, the first-order models could then be improved upon when needed by more accurate descriptions (NWP), or when resources allow (computation power, time, etc.).

In Section 2, we introduce the area of study, highlight the most infrasonically active volcanoes in the region, and present the datasets we use to compare with our models. In Section 3, we introduce our methodology to estimate year-long infrasound back-azimuth deviations, and the different atmospheric and ray-tracing propagation schemes we consider. In Section 4, we summarize the annual back-azimuth prediction results, compare them with the multi-year dataset, and measure the accuracy of each model on a year-long time window. In Section 5 we discuss the results and the limitations of our approach, and pinpoint some interesting results. Finally, in Section 6 we review our findings and suggest the next steps forward.

2 THE VANUATU ARCHIPELAGO VOLCANIC ARC

Along the South Vanuatu Trench in the South Pacific Ocean, more than 80 islands stretch northeastward to form the Vanuatu archipelago volcanic arc (Figure 1) (Eissen et al. 1991; Simkin & Siebert 1994). The active volcanoes of this archipelago have a rare diversity of eruptive styles which range from effusive to highly explosive, hence becoming a valuable laboratory for volcanologists to better understand eruption dynamics (Beaumais et al. 2016; Coppola et al. 2016; Meier et al. 2016; Vergniolle & Métrich 2016).

As shown in Coppola et al. (2016), from 2000 to 2015 Yasur (Tanna island), Lopevi (Lopevi island), Ambrym (Ambrym island), Lombbenben (Ambae island, herein referred as Ambae) and Mont Garet (Gaua island, herein referred as Gaua; see also (Park et al. 2021)) volcanoes were the most active volcanoes of Vanuatu archipelago. Although most local multi-parameter studies in the region target Yasur due to its essentially continuous explosive activity (Maher et al. 2022; Marchetti et al. 2013; Matoza et al. 2022a; Meier et al. 2016; Spina et al. 2016).

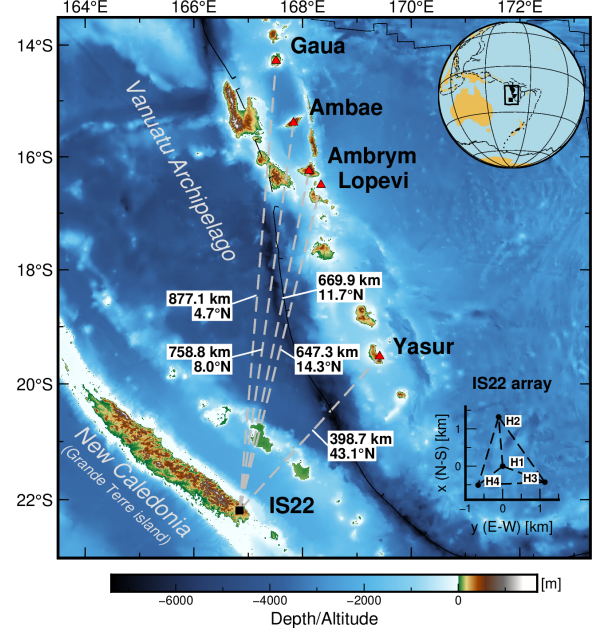


Figure 1. Study region (see box in upper right inset), comprising the Vanuatu archipelago and the main island of New Caledonia (Grande Terre). Black square: location of IS22, New Caledonia. Red triangles: location of the most active volcanoes; names on right. Gray dashed lines: great-circle distances and azimuths from IS22 to each volcano (annotated). Lower-right: IS22 array geometry in Cartesian coordinates (km).

2.1 IS22: multi-decadal long-range volcanic infrasound records

At ~400 km southwest of the Vanuatu archipelago, the IMS infrasound station IS22 (Grande Terre island, New Caledonia) has been recording signals from Vanuatu volcanoes since 2003 (Figure 1). The station IS22 (or I22FR) is composed of four MB2000 microbarometers separated by ~1 km (Figure 1, bottom right panel). Each microbarometer has a flat frequency response (within 3 dB) between 0.01 and 8 Hz, with noise levels less than 2 mPa between 0.02 to 4 Hz, and a sampling frequency of 20 Hz (Marcillo et al. 2012).

Coherent infrasound signals propagating across IS22 can be extracted from non-coherent infrasound with the Progressive Multi-Channel Correlation (PMCC) time-domain method (Cansi 1995). The PMCC method can obtain the coherent signal's mean frequency, trace velocity, amplitude, and azimuth remarkably well under low signal-to-noise ratios (<0.5) (Cansi 1995; Matoza et al. 2013). Once a passing wave is identified, the PMCC groups coherent waveforms with similar plane-wavefront properties across sensors into what we call a detection (Cansi & Klinger 1997).

Among many natural and human-made sources detected by IS22 (e.g., microbaroms, surf, mining explosions, etc.; see Figure 2), the persistent eruptive activity of Yasur volcano (19.532°S, 169.447°E; 361 m summit; distance ~400 km), and the combined eruptive sequences of Ambrym volcano (16.25°S, 168.12°E; 1334 m summit; distance ~700 km), and Lopevi volcano (16.507°S, 168.346°E; 1413 m summit; distance ~700 km) consistently appear during the last ~20 years (2003–2022; see Figure 2). These incessant detections have provided an important test-bed to compare and evaluate the accuracy of the stochastic (HWM/MSISE) and Numerical Weather Prediction atmospheric models (NRL-G2S and ECMWF) (Le Pichon et al. 2005a,c; Drob

et al. 2003; Le Pichon et al. 2006; Antier et al. 2007; Assink et al. 2014a), to develop passive atmospheric inversion techniques targeting high-altitude winds (Le Pichon et al. 2005a,c; Lalande et al. 2012), to propose improvements for the IMS infrasound network, and test new techniques for remote detection of volcanic eruptions (Le Pichon et al. 2010, 2009b; Tailpied et al. 2017; Morelli et al. 2022).

2.2 Open access infrasound data products

In this study, we use open access infrasound data products developed by Hupe et al. (2022), which represent summaries of array processing detection lists rather than the raw lists. These data products started as the result of synthesizing 2003 to 2020 IMS infrasound detections produced from PMCC array processing with a 26-band logarithmic-spaced parametrization, and since then have been updated yearly. The open access data products (see Hupe et al. 2021) use a quality value to gather the most robust PMCC detections and classify them into four specific frequency ranges, which target the most common natural and human-made phenomena: 0.02–0.07 Hz “very low frequency” (e.g., mountain associated wave infrasound), 0.15–0.35 Hz “low-frequency microbarom”, 0.45–0.65 Hz “high-frequency microbarom”, and 1–3 Hz “high-frequency” (e.g., volcanic eruptions and surf).

Here, we will use the “high-frequency” (1–3 Hz) open access products (herein, “PMCC products”) for IS22 covering from years 2003 to 2023 (Figure 2; see also Figure 1 in Supplementary Information), as most of the infrasound at IS22 from Lopevi/Ambrym and Yasur volcanoes centers around 1 Hz and 2 Hz, respectively (Antier et al. 2007; Assink et al. 2014a; Le Pichon et al. 2005a; Morelli et al. 2022).

For comparison and validation of these data summary products, we compare with full array detection lists using 15-band (2003–2017) (Matoza et al. 2013; Ceranna et al. 2019) and 26-band (2003–2023) (Hupe et al. 2022) PMCC parametrizations in the Supplementary Information (SI) (see SI Figures 4 to 8, and 11 to 13). Unlike the summaries by Hupe et al. (2022), these detection lists are the direct output of PMCC array processing of the waveforms recorded at the station IS22.

2.3 Chronological and “folded” observations

Volcanic, surf, and possibly mining infrasound (“anthropogenic”), are the three main types of “high-frequency” (1–3 Hz) detections at IS22 from 2003 to 2022 (see labels in Figure 2a). Non-volcanic infrasound falls at much higher back-azimuths than Yasur ($\sim 43^\circ$) and the “Ambrym group” (i.e., Ambrym/Lopevi/Gaua/Ambae; $\sim 5^\circ$ – 14°). The distinct quasi-continuous infrasound around the back-azimuth of Yasur roughly resembles the shape of “bottom half sinusoids” during summer months (Figure 2b), with periods of one year. The detections around the back-azimuth of Ambrym appear more sporadically, resembling the slopes of a sinusoid in years with more detections (e.g., 2004–2008 in Figure 2c).

The periods of volcanic activity catalogued by the Vanuatu Meteorology and Geo-hazards Department (VMGD) (Figures 2b,c in gray vertical lines and shaded areas; also by relative Real-time Seismic Amplitude Measurement (RSAM) from a couple of available stations near Yasur volcano in Figure 2b) serve as valuable complementary observations (e.g., McKee et al. 2021a,b; Matoza et al. 2022a). Their observations indicate that overlapping of infrasound sources among the Ambrym group seems feasible. In particular, during the second half of 2010 (Figure 2c), a large group of

detections appears around the azimuth of Gaua volcano, coincident with a long eruptive period that occurred from September 2009 to July 2010 (Bani et al. 2016).

Sorting the detections by day of year (i.e., “folding” into a year; Figure 2d,e,f), shows that most of the 2003–2022 IS22 infrasound detections come from the directions of Yasur and the Ambrym group volcanoes. The abundant detections that chronologically resemble “bottom half sinusoid” curves from the back-azimuth of Yasur (Figure 2a,b) are sorted into a “capped arc” now (Figure 2e). This feature shows up between October and March (Figure 2e; days ~ 280 to 365, and 1 to ~ 100), with minimum values by the end of December to the start of January, and transition periods from March to April (negative to positive azimuth deviations) and October to November (positive to negative). Relatively large groups of detections also appear sporadically between May and August, decoupled from the seasonal deviation trend (i.e., the “capped” part of this arc), with azimuth deviations ranging from approximately -4 to $+6^\circ$ (Figure 2e). The “folded” Ambrym group (Figures 2d,f) shows detections resembling the sides of a “main arc” around Ambrym/Lopevi. In this case, the features are less clear, as the numbers of detections are much lower than Yasur’s case. However, Figure 2c does suggest sinusoidal back-azimuth variation during periods of higher number of detections (e.g., 2004–2008). Similarly, we consider it feasible that the traces of a “secondary arc” exist centered near Ambae/Gaua back-azimuths (approximately -3 to -5° below the main arc). The hypothesis of a secondary arc stems from the fact that, if Ambae and/or Gaua produced detectable infrasound during shorter periods of time (e.g., in the middle of 2010), these detections should be equally influenced by the travel path effects that make Ambrym/Lopevi detections have a sinusoidal back-azimuth deviation through the year. For both cases, most of their detections appear from March to April and August to October, while decoupled groups of detections appear from June to August, similar to the case of Yasur volcano (Figure 2e).

3 ANNUAL LONG-RANGE PROPAGATION MODELS

3.1 Methodology

We attempt to model the bulk seasonal to daily effects to first-order (e.g., the “capped arc” and “main arc” features; Figure 2e), which could provide valuable insights and potentially seasonal predictions of the azimuth deviation from each source. To do so, we use the methodology introduced by De Negri & Matoza (2023) to simulate the observed detections at IS22 from the locations of Yasur and Ambrym volcanoes (see the “ARCADE” open-source repository link in Acknowledgments) in year-long time windows.

The ARCADE procedure (De Negri & Matoza 2023) is designed to automatically look for ground intercepts (arrivals) at pre-defined receiver locations (stations) coming from an arbitrary number of source locations (volcanoes), at specified dates and times. By default, it couples empirical climatologies (HWM14/MSIS2.0) (Drob et al. 2015; Emmert et al. 2020) and models infrasound propagation with 3D ray tracing (infraGA) (Blom 2020; Blom & Waxler 2012, 2017). The atmospheric models can also be discretized as range-independent (layered spherical) or range-dependent (3D grid for the area), allowing different levels of detail in the specifications. The modularity of this approach permits using different atmospheric specifications that we will test in terms of accuracy.

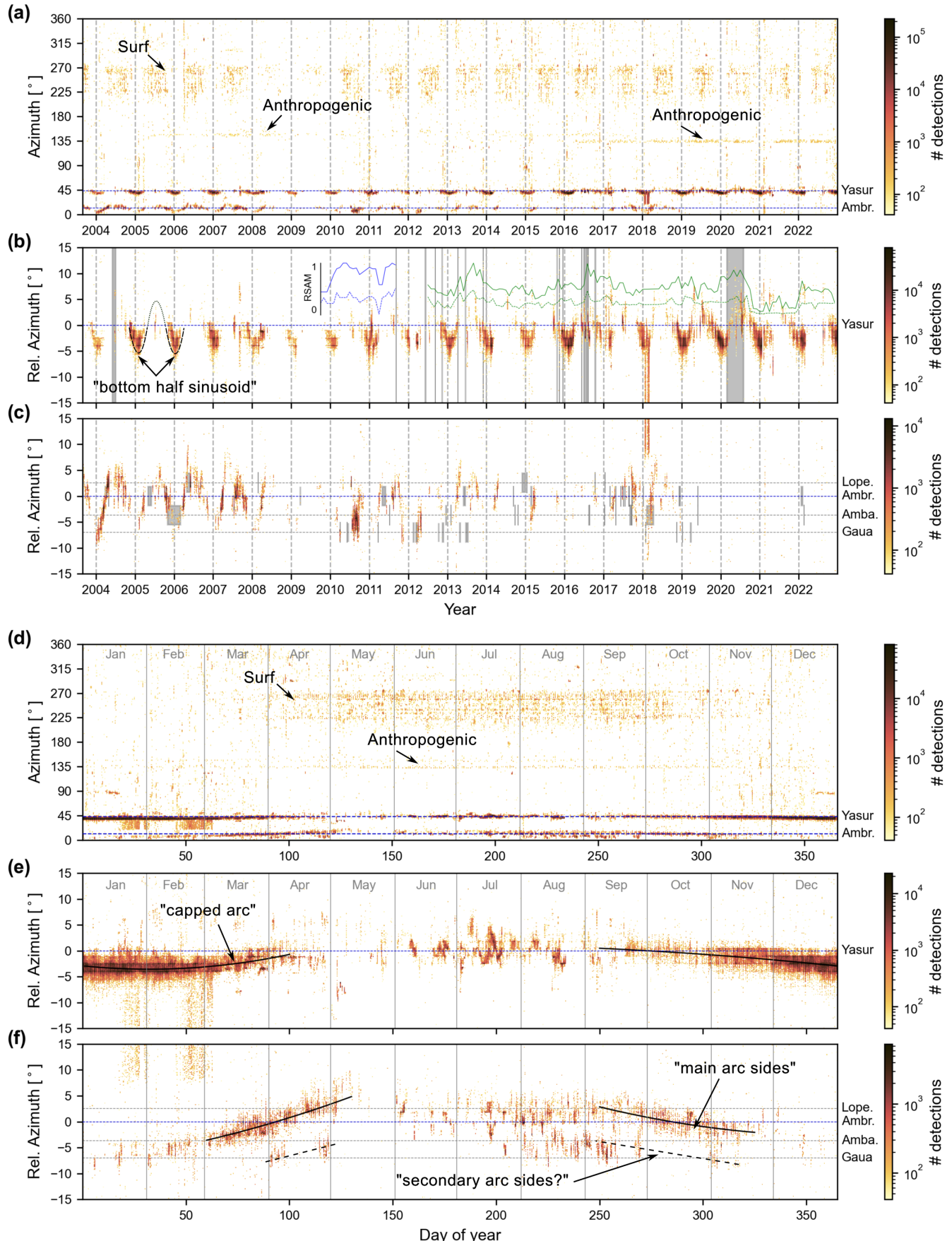


Figure 2. Infrasound detections at IS22 from mid-2003 through 2022 (Hupe et al. 2022). (Caption continues on next page.).

Figure 2. (Previous page.) (a) 2D color-shaded histogram of detections by year (*x*-axis) vs. azimuth (*y*-axis), colored by the number of detections in each bin. Each 2D bin is 277.4 hours (~ 12 days) wide and 1.8° high. Horizontal dashed blue lines and annotations indicate the back-azimuths from IS22 to Yasur and Ambrym volcanoes. (b) and (c) show zooms around Yasur (43.1°), and Ambrym (11.7°) azimuths, respectively; an insert in (b) shows the minimum (dashed) and maximum (continuous line) relative values of the Real-time Seismic Amplitude Measurement (RSAM) from the Vanuatu Meteorology and Geo-hazards Department stations, YAS (blue) and YASH (green); dashed gray lines in (c) depict relative azimuths of Lopevi, Ambae, and Gaua volcanoes with respect to Ambrym. A reference black line labeled as “bottom half sinusoid” in (b) shows how the detections roughly align around a half-sinusoid with a period of one year. The continuous part of the line indicates where there is data to support the hypothetical shape, while the dashed part is only a reference to indicate the periodic behavior of the azimuthal deviations. In (c) and (d), the active periods of each volcano (Vanuatu Meteorology and Geo-hazards Department observations) are shown as solid gray vertical lines (single day event) and solid gray shaded areas (multi-day event). (d) similar to (a), but the data for all years are collapsed and folded into a single year and plotted by day-of-year. In (d), the bin size is 14.6 hours wide by 1.8° high. (e) and (f) are again zooms around the azimuths of Yasur and Ambrym, respectively; bin size is 14.6 hours wide by 0.3° high. A sinusoid-like black line in (e) indicates a year-long oscillation of the “bottom half sinusoid” introduced in (b), roughly following the multi-year stacked data. The “capped arc” shown here follows a second-degree interpolated curve of manually selected data that approximately follows a seasonal behavior (see SI Figure 2). In (f), the labeled “main arc sides” curves show the interpolations of selected observations that roughly match the seasonal behavior observed in (c), attributed to Lopevi/Ambrym back-azimuths. Black dashed lines, labeled as “secondary arc sides?”, are manually traced slopes show where possible Ambae/Gaua volcanic infrasound sporadically appears. See SI Figure 3 for an unlabeled version of this figure.

3.1.1 Hybrid model

The empirical climatologies are stochastic models based on interpolations of historical data collections, which are improved over time as new global datasets are gathered. This means that they are robust atmospheric descriptions, but smooth out smaller spatiotemporal changes that occur in the lower parts of the atmosphere (troposphere/lower stratosphere), as the Quasi-Biennial Oscillation (QBO) (Anstey & Shepherd 2014; Kidston et al. 2015) and Sudden Stratospheric Warming (SSW) events (Drob et al. 2010; Drob 2019; Assink et al. 2014a; Smets et al. 2016). To try to account for this issue, ARCADE (De Negri & Matoza 2023) does include the option of using a hybrid model that merges the European Centre for Medium-Range Weather Forecasts reanalysis v5 (ECMWF ERA 5, or ERA 5 for simplicity) descriptions (horizontal winds, pressure, and temperature) below ~ 78 km altitude, with pure (raw) empirical climatologies at higher altitudes. The ERA 5 reanalysis models, available from 1959 to the latest processed forecast model, describe the lower atmosphere in greater detail, accounting for specific year and date-time variations with a minimum time step of one hour and a minimum spatial step of 31 km (Bell et al. 2021).

The hybrid models will be the only type able to distinguish each year, as the empirical climatologies are interpolations of multi-year data into one characteristic year. These models will therefore be more accurate in representing transient non-seasonal changes, in detriment of representing repetitive (seasonal) phenomena in a multi-year scale.

3.1.2 Perturbed climatologies

One possible approach to account for phenomena not represented in the empirical climatologies is to generate multiple fine-scale variations of the average descriptions (multiple statistical realizations) simulating fine-scale structure or gravity wave effects (e.g., Assink et al. 2014a; Smets et al. 2016). Here, however, we take a simpler parametric approach, incorporating the addition of a Gaussian wind jet (Jones 1986) centered at a specific altitude, which creates perturbations of the range-independent climatological (HWM14/MSIS2.0) descriptions. This simplified type of perturbation is intended to adequately compensate for missing fine-scale structure that is not included in either hybrid atmospheric specifications nor empirical climatologies, without having to resort to a full gravity-wave model parameterization and multiple ensemble realizations. This approach, which was further motivated by De Negri & Matoza (2023), aims to sufficiently “nudge” the profiles to form a duct when the observations imply that the duct existed, yet the unperturbed profiles do not predict arrivals.

3.1.2.1 Static perturbation Originally, De Negri & Matoza (2023) defined the Gaussian perturbation parameters after manually analyzing effective wind profiles for the cases studied. The parameters of altitude, width, and amplitude that would increase the horizontal winds were set to avoid unrealistic arrivals. In this type of perturbation, the Gaussian enhancement is fixed at 40 km altitude by default, increasing the along-path winds with an amplitude, c_0 , that corresponds to a 30% of the maximum along-winds (m/s) within the 30 to 50 km altitude limits (see Eq. 1; De Negri & Matoza 2023).

$$\tilde{c}(h) = c_0 e^{-(h-h_0)^2/(2\Delta h^2)} \quad (1)$$

where Δh is the width (km), and h_0 is the central altitude (km) at which the perturbation is applied. That is, the amplitude (c_0) is centered at a fixed altitude (h_0), with a ± 10 km width (Δh). This perturbation (\tilde{c}) is applied only when positive along-path stratospheric winds are present, defaulting to raw (unperturbed) empirical climatologies when not. However, this choice of perturbation has likely underestimated the number of stratospheric arrivals (De Negri et al. 2022; De Negri & Matoza 2023), while the numerous observations from Yasur have been regarded as dominantly stratospheric (e.g., Le Pichon et al. 2005a; Antier et al. 2007; Assink et al. 2014a).

3.1.2.2 Adaptive perturbation Attempting to approximate the higher amplitude and smaller oscillation lengths of typical gravity wave perturbations (e.g., Green et al. 2011; Drob et al. 2013; Smets et al. 2014), we tested several reasonable parameter modifications of Eq. 1, to examine how the altitudes, widths, and amplitudes of perturbations could increase stratospheric arrivals at IS22. After these preliminary experiments we incorporated a second type of perturbation based on Eq. 1. We decided to (1) increase the amplitude perturbation (c_0) to a 90% of the maximum along-wind speeds from 30 to 60 km (i.e., up to ~ 16 m/s mean increase during along-wind days), (2) reduce the width (Δh) to 1 km, and (3) center the perturbation at a height (h_0) that follows the local maximum per day and time (see SI Figure 14 and SI Table 1). These perturbations, despite not being actual gravity-wave perturbations, better resemble the distortion length of one gravity wave oscillation and the maximum perturbation value it could have (e.g., Green et al. 2011; Drob et al. 2013; Smets et al. 2014). Additionally, we apply the adaptive perturbation proportional to the factor R (see Eq. 2) to the zonal winds (u), and proportional to the factor $1 - R$ to the

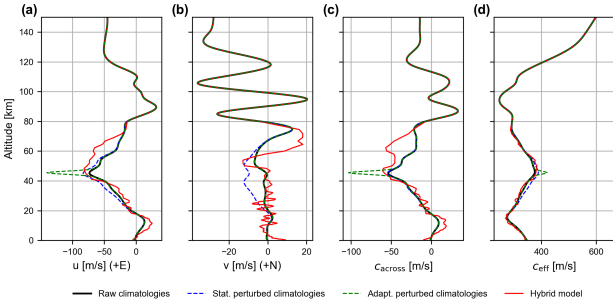


Figure 3. Example of mean horizontal winds vs. altitude for 15 January 2019 at 00:00 UTC from Yasur to IS22 (x -axis) in steps of 0.5 km altitude (y -axis), calculated with climatologies (black line), static perturbed climatologies (blue dashed line), adaptive perturbed climatologies (green dashed line), and the hybrid model (red line) descriptions. (a) Zonal winds (positive towards the east). (b) Meridional winds (positive towards the north). (c) Crosswinds (positive towards north-east). (d) Effective sound speed considering the along-path winds and temperature in altitude.

meridional winds (v), thus guaranteeing a perturbation that follows the actual wind magnitude ratios (Figure 3).

$$R = \left| \frac{u(h_0)}{\sqrt{u(h_0)^2 + v(h_0)^2}} \right| \quad (2)$$

To summarize, in this study we will use “raw climatologies”, “hybrid models”, “static perturbed climatologies” (default perturbation), and “adaptive perturbed climatologies” (last introduced) to obtain the atmospheric descriptions for each modeled case (Figure 3)

3.2 Propagation models

After inspecting the multi-year (2003-2022) set of detections (Figure 2a,b; also SI, Figures 4 and 5), we decided to calculate year-long infrasound propagation models corresponding to 2004 for Ambrym volcano (herein, “2004 Ambrym”) and 2019 for Yasur volcano (herein, “2019 Yasur”). These two years have numerous candidate detections for each case, presenting complete datasets to compare with the models.

We cover all the possible combinations with this methodology, calculating six different models per volcano and year: range-independent with raw climatologies, range-independent with static perturbed climatologies, range-independent with adaptive perturbed climatologies, range-independent with hybrid model, range-dependent with raw climatologies, and range-dependent with hybrid model.

With each model, an iterative ray-tracing search is automatically performed for every day of the year, every six hours (00:00, 06:00, 12:00, and 18:00 Coordinated Universal Time (UTC)). The source-year-day-time runs try to estimate the back-azimuth deviation using arrivals near enough IS22 (< 5 km), with turning heights up to ~ 120 km (thermospheric). We define the back-azimuth deviation as the mean difference between the true back-azimuth and the modeled back-azimuth of the considered arrivals, which mostly come from stratospheric and lower thermospheric ducts (De Negri & Matoza 2023).

Using the year-long sets of back-azimuth deviations for each model, we build year-long 1D-spline interpolations based on the daily means (Figure 4, see green lines for each model). The interpolated curves will serve to compare models, and more importantly,

to calculate the accuracy of each model when compared with the observations.

All models managed to produce a mostly complete set of arrivals to calculate the back-azimuth associated with each source-year-date-time combination. However, the range-dependent, raw climatology model for Ambrym volcano failed to produce ground intercepts (arrivals) near enough IS22 (Figure 4k). We interpret this issue as the indication of an unstable propagation model, where the ray propagation becomes too sensitive to small changes in the launching parameters. However, further clarifications will be part of future research as we gathered enough results to complete the comparison with the datasets.

4 RESULTS

4.1 Regional winds and detectability

Yasur and Ambrym groups of detections have a marked yearly oscillating back-azimuth behavior. This phenomenon correlates well with the yearly regional zonal wind patterns, which are clearly captured by climatology-based and hybrid atmospheric models (e.g., Figure 5 for winds during 2019).

Infrasound propagating from Ambrym and Yasur to IS22 (Figure 1) will encounter eastward stratospheric (~ 30 -60 km) zonal winds from April to October and westward winds from November to March (e.g., Figure 5a,c,e,g). Yasur infrasound will find a sustained propagation duct when westward zonal winds occur, whereas the eastward winds create upwind propagation conditions, making them almost undetectable (e.g., Figure 5b,d,f,h). At the same time, sources north from IS22 (i.e., Ambrym/Lopevi/Gaua/Ambae), will have no clear favorable stratospheric ducting conditions. Instead, they will suffer high crosswinds during prevalent eastward/westward zonal winds. However, at thermospheric altitudes (~ 110 -120 km), there is another theoretical duct that could enhance infrasound propagation to IS22 (Figure 5b,d,f,h). During wind regime transition periods (seasonal equinoxes), characterized by weak zonal winds (e.g., see wind profiles from March-April and September-November in Figure 5), the minimal crosswinds could enable infrasound refracted at thermospheric heights to be more detectable, coincident with the times when most of the detections from Ambrym/Lopevi azimuths appear (Figure 2f).

4.2 Observations: interpretations and shortcomings

4.2.1 Seasonal arcs and transient phenomena

The shared arc-like (sinusoidal) behavior of the modeled detections (Figures 4 and 5) suggests that the candidate detections coming from Yasur and Ambrym back-azimuths (Figure 2) are mainly due to the effect of the seasonal stratospheric zonal winds.

The near-continuous volcanic explosive signals from Yasur to IS22 shows as “bottom half sinusoids” or “capped arc” features due to low detectability during upwind conditions in winter (eastward winds; e.g., Figure 5 for 2019). Transient stratospheric westward ducts during dominant eastward winds, linked with Sudden Stratospheric Warming events in the region (Assink et al. 2014a) (e.g., Figure 5b near July and September for 2019), allow detections to be seen for days to weeks in a row (e.g., Figures 4g,i for Ambrym and Figures 4h,j for Yasur near day 170).

Most of the detections of the “Ambrym group” occur during

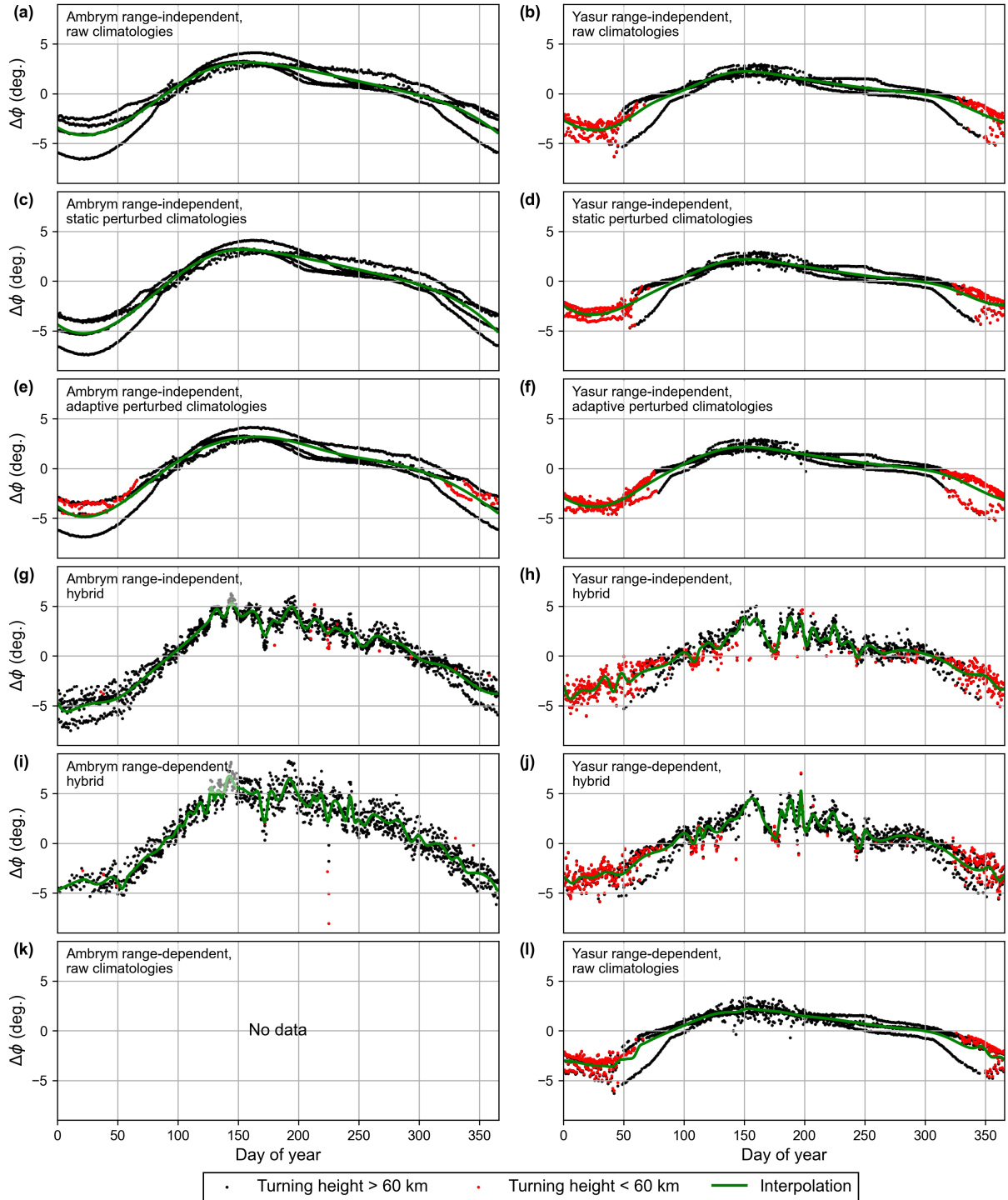


Figure 4. Modeled arrival relative back-azimuths (centered around each volcano) colored by turning height threshold (see bottom legend) for all times (00:00, 06:00, 12:00, and 18:00 UTC). Red dots: arrivals with turning height less than 60 km (usually near 30-50 km). Black dots: arrivals with turning height more than 60 km (usually near 110-120 km). Green line: 1-D spline interpolations of the daily mean deviations, with a smoothing factor of 10 (less smooth) for the climatology-based models, and 50 (more smooth) for the hybrid-based models. Both curves were calculated using interpolations tools included in the module Scipy of the Python 3.9 libraries (splrep and splev), which are based on the FITPACK Fortran libraries (Dierckx 1995). Left subplots: Ambrym cases. Right subplots: Yasur cases. (a) and (b): range-independent, raw climatologies. (c) and (d): range-independent, static perturbed climatologies. (e) and (f): range-independent, adaptive perturbed climatologies. (g) and (h): range-independent, hybrid. (i) and (j): range-dependent, hybrid. (k) and (l): range-dependent, raw-climatologies (note that (k) has no results).

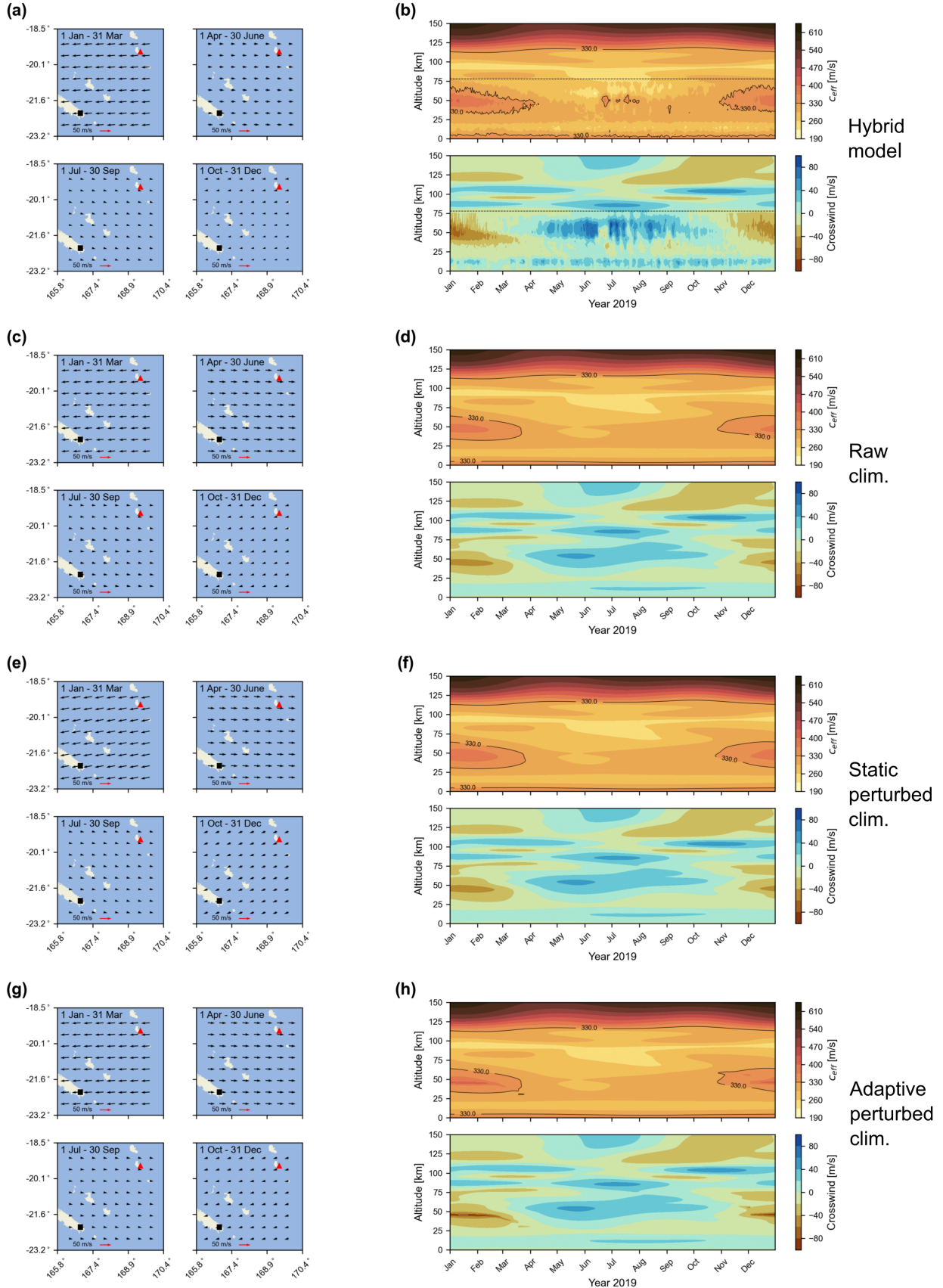


Figure 5. Seasonal atmospheric conditions at 00:00 UTC from 1 January 2019 to 31 December 2019. (Caption continues on next page.).

Figure 5. (Previous page.) (a) and (b) Captured by a hybrid model combining ECMWF ERA 5 atmospheric specifications below ~ 80 km with HWM14/MSIS2.0 from ~ 80 to 150 km. (c) and (d) Captured only by the empirical climatologies (HWM14/MSIS2.0). (e) and (f) Captured by the empirical climatologies with a Gaussian enhancement of 30% in the along-path winds centered at 40 km (i.e., “static perturbed”). (g) and (h) Captured by the empirical climatologies with a Gaussian enhancement of 90% along-path wind centered at the maximum along-path wind height between 30 and 60 km at each day and time (i.e., “adaptive perturbed”). (a), (c), (e) and (g) Mean horizontal wind vectors for each set of atmospheric descriptions from 30 to 60 km for four characteristic times of the year: 1 January to 31 March (upper left), 1 April to 30 June (upper right), 1 July to 30 September (lower left), and 1 October to 31 December (lower right). In each case, a red arrow indicates a scale of 50 m/s (all panels have same scale for vector lengths). Black square: IS22; red triangle: Yasur. (b), (d), (f) and (h) Mean along-path effective sound speed (top) and crosswinds (bottom) for each set of atmospheric descriptions as a function of altitude (0 to 150 km) from Yasur to IS22 during 2019.

transition zonal wind regimes (March to April and August to October), which means that the bulk of the Ambrym group happens during a weakened or non-existent stratospheric duct. Indeed, the atmospheric effective sound speeds profiles for the region suggest that these candidate detections are enabled by the thermospheric duct (~ 110 - 130 km), whereas the sinusoidal azimuthal deviations are caused by the crosswinds due to the seasonal zonal winds at stratospheric heights (e.g., see Figure 5). As confirmed by the models, the crosswinds imposed on the propagating signals from Ambrym result in stronger azimuth deviations due to their North-to-South propagation path (Figure 1). The peak-to-peak asymmetry in the modeled back-azimuths and the observed candidate detections indicates stronger westward (summer) than eastward zonal winds (winter) in the region.

It is likely that the “second arc” present in the folded observations (Figure 2d,f) is an overlap of candidate detections from Gaua and Ambae volcanoes. The models indicate that the daily variations (Figure 4) are not higher than the back-azimuth differences from Ambrym/Lopevi and Gaua/Ambae (~ 7 - 4 °). However, further modeling and comparison with other datasets are required to clarify this hypothesis.

4.2.2 Artifacts and frequency bands

At the start of 2018, we observe two groups of detections spanning from ~ 10 to 45 ° that appear to be artifacts (Figure 2a; also Figure 2d,e,f at the end of January, February, and the start of March). These detections are also present in the 26-band PMCC dataset during the same time window (SI, Figure 4), and were likely produced by temporary station issues, possibly due to a malfunction of one of the sensors. The dataset also shows the formation of azimuthal bands of detections at ~ 1.25 ° steps for the Yasur group of detections (Figures 2b and 2e) that appear to be artifacts. They are present in the 26-band PMCC data (SI, Figures 4b,c,e,f) but not the 15-band PMCC data (SI, Figure 5b,c,e,f) and are likely a processing artifact effect of the 26-band configuration.

4.3 Comparison with year-long and multi-year datasets

We aim to compare the back-azimuth interpolated model curves from year-long infrasound back-azimuth deviation estimations at IS22 (see Figure 4), with the high-frequency (1–3 Hz) infrasound products (Hupe et al. 2021) for the years 2004, 2019, and the whole

stacked (folded) multi-year time window (2003-2022). However, the ever-present non-volcanic overlapping sources (clutter), and propagation scatter effects make the comparison of a single interpolated curve difficult. Therefore, before calculating the error estimation of each model, we need to apply reduction techniques to the observations to represent the average behavior of the candidate (volcanic) detections.

4.3.1 Data reduction

To reduce clutter, we first select the high-frequency products (Hupe et al. 2021) that have a quality parameter $Q > 0.4$ (Hupe et al. 2022). By default the products are composed of groups of detections with a size above 40 (Hupe et al. 2022), while for the other two datasets we set a minimum size threshold of 10 for each group of detections (families). Then, we consider only the detections with back-azimuths within ± 10 ° around the true direction of each volcano. We calculate the mean of the selected detections within the interval bounded by the 10th and 90th percentiles for the back-azimuth distribution in 7-day consecutive time windows, producing the values that we use to compare with the modeled interpolations. The 7-day means will be the reference data to compare with the model interpolations, allowing us to measure the performance of the models.

4.3.2 2004 Ambrym and 2019 Yasur comparison

The interpolated curves, centered at each back-azimuth, generally follow the most numerous candidate detection groups for both 2004 Ambrym and 2019 Yasur cases (Figures 6a,c). The 7-day 90% confidence reduced observations are a much more clear indication of the fitting of each model to the observations (Figures 6b,d).

For 2004 Ambrym case, the reduced observations have a large negative deviation (~ -7.5 °; Figure 6b) at the start of the year, followed by a linear increase from days ~ 40 to 120, and reaching values of ~ 2.5 ° towards the middle of the year (day ~ 150). The second half of the year (day ~ 200 - 300) has fewer detections, which follow a negative slope in a more scattered manner than the first half. The match between the observations and the modeled results is good from days ~ 40 to 120 for all models, both following a similar rate of back-azimuth change in time. However, the observed deviation values are underestimated by all models in the beginning of this period (days ~ 40 - 120), while the hybrid model interpolations (blue lines) are the only curves that follow the higher slope of the transition from negative to positive deviations from days ~ 100 to 120. As previously hypothesized, the back-azimuth variability of the detections is better portrayed by the hybrid predictions, which are able to follow detections with negative deviations during periods of positive deviations in the empirically constrained climatologies (e.g., day ~ 180). The frequencies of the reduced observations remain near 1 Hz in most cases.

For 2019 Yasur case, the reduced observations show a good agreement with all the interpolated curves when the westward stratospheric duct is present (days 1 to ~ 100 and ~ 300 to 365; Figure 6d). The hybrid models again seem to better follow groups of detections that are outliers from the seasonal predictions (e.g., day of year ~ 180 , with ~ 1.8 Hz, and azimuth deviation of ~ 0 °). Interestingly, from days ~ 250 to 320, the back-azimuths are underpredicted by all the models. The reduced observations show distinct frequency changes through the year, periods of higher frequencies (~ 1.8 Hz) happen at the beginning/end of the year and in

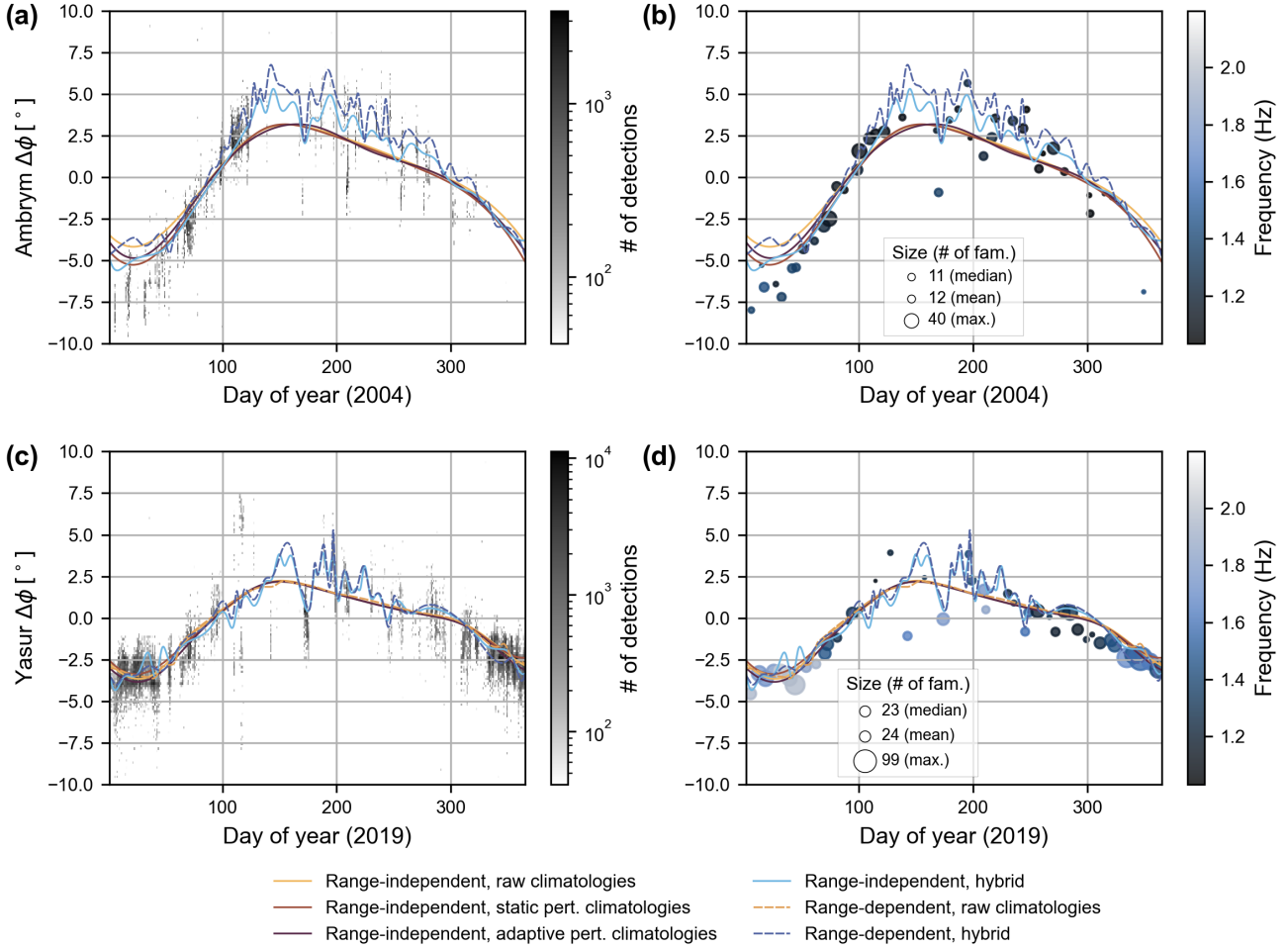


Figure 6. Modeled predicted back-azimuth deviations compared to IS22 observations (high-frequency 1–3 Hz products of Hupe et al. (2021)). (a) and (c) 2D binned observations colored by number of detections (see Figure 2) vs. the interpolated curves of the models colored by type (see Figure 4) for 2004 Ambrym and 2019 Yasur, respectively. (b) and (d) 7-day means of reduced observations within 90% confidence interval from the mean as colored circles by mean frequency, with circle size by number of “families” (a measure of time-frequency span of the signals) vs. the same interpolations.

the middle of the year, while lower frequencies (~ 1.2 Hz) appear between these periods. Following the hybrid model results (Figure 4h,j), we interpret this effect as the relation between turning height and transmission loss. Favorable summer stratospheric ducts and transient stratospheric along-path winds during winter, which are likely driven by the QBO effects at these southern tropical latitudes (Anstey & Shepherd 2014; Assink et al. 2014b), allow higher frequencies to reach IS22 (shorter travel path). On the other hand, weak stratospheric ducting conditions force most ray-paths to rely on the higher altitude thermospheric duct (~ 110 – 120 km), lowering the mean frequencies of the arrivals at IS22.

4.3.3 Ambrym and Yasur multi-year (2003–2022) comparison

The models show general agreement with the multi-year observations again from days 1 to ~ 100 , and ~ 250 to 365 (Figure 7). However, the linear-like clusters of detections (i.e., frequency bands; see Section 4.2.2) clearly appear in steps of $\sim 1.25^\circ$ around the back-azimuth of Yasur, skewing the overall statistics for this group (Figure 7c). Fortunately, the model comparison with the 15-band 2003–

2017 dataset (SI, Figure 8) shows that the most important characteristics of the back-azimuth changes are still well represented.

The hybrid models, despite their specific time dependency, better represent the slope of the transitions from negative to positive deviations (e.g., day 100–120).

Between day ~ 120 and ~ 250 , the possible Gaua/Ambae group of detections (see Section 2.3) appears under Ambrym’s modeled deviations (Figure 7a) from $\sim -2.5^\circ$ to -7.5° . This group falls outside the interval bounded by the 10th and 90th percentile of the back-azimuth distribution in the 7-day rolling window, therefore it is erased from the reduced representation (Figure 7b). Their frequency content (~ 1.6 Hz) is slightly higher than most of the detections (~ 1 to 1.4 Hz), with only one notable group that has clearly higher frequencies than the rest (~ 1.8 – 2.2 Hz, near day 200). This suggests mixing of detections from transient stratospheric ducts with detections from thermospheric ducts (Figure 7b). Additionally, if these detections are indeed from Gaua/Ambae, this could indicate a higher characteristic source frequency than Ambrym (~ 1 Hz).

More outlier detections build up in the multi-year view for Yasur’s comparison (Figure 7d; days ~ 100 to ~ 250). These detec-

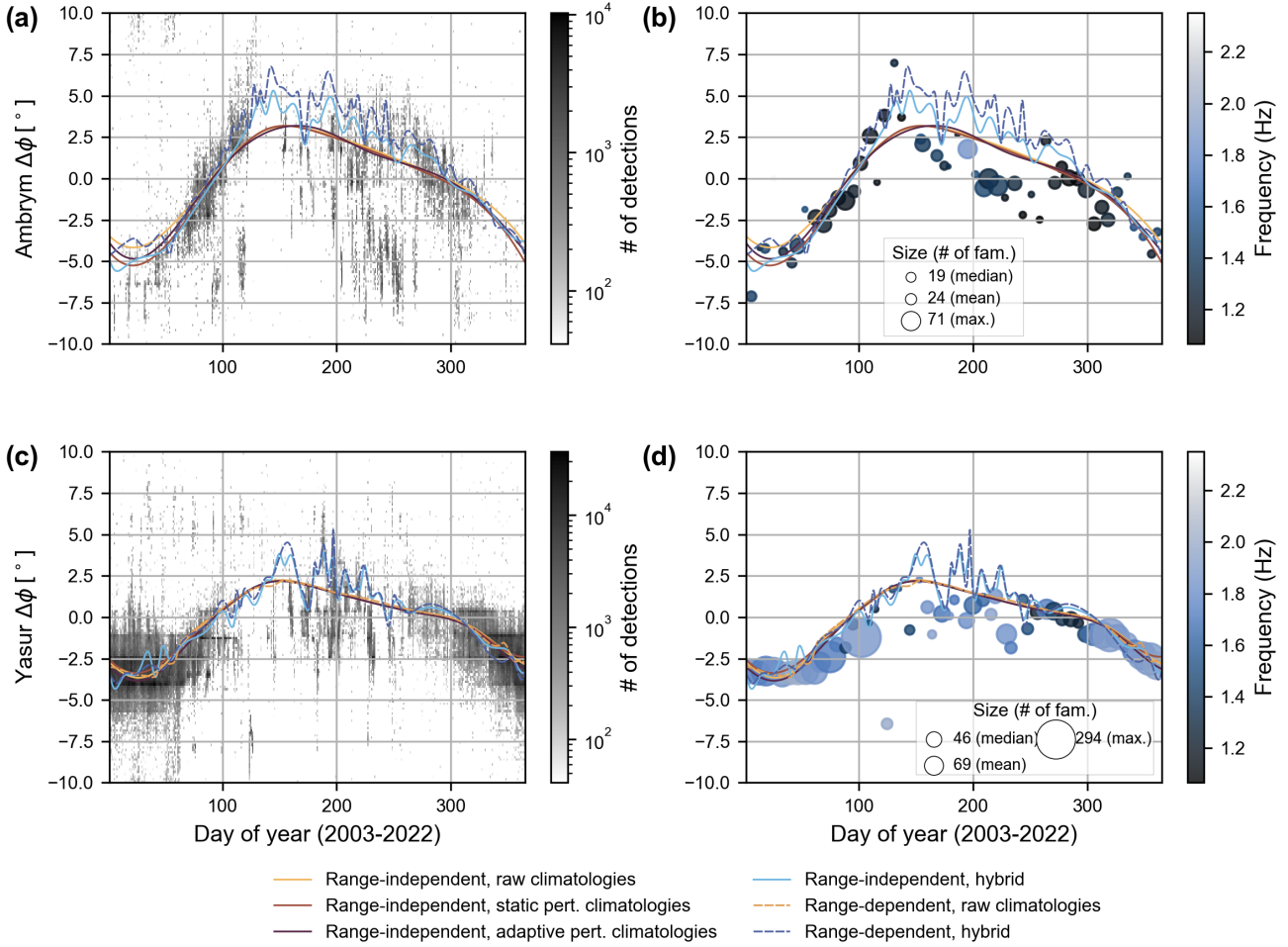


Figure 7. Same as Figure 6, but including all of the multi-year observations from 2003 to 2022 (1–3 Hz products of Hupe et al. (2021)) for Ambrym (a, b) and Yasur (c, d).

tions show smaller deviations than predicted by the climatology-based models, only partially matched by the hybrid curves. During days ~ 280 to ~ 320 groups of less numerous, lower frequency detections (~ 1.2 to 1.4 Hz) transition towards more numerous, higher-frequency groups (~ 1.8 to 2.2 Hz). However, this frequency effect is clearly visible in the 15-band 2003–2017 stacked analogous comparison (see SI Figure 8), resembling the case of 2019 for Yasur (Figure 6d).

4.3.4 Accuracy of the models

Up to this point, we have shown that the models are qualitatively comparable with the reduced datasets (Figures 6, 7). Now, we formulate a simple monthly and yearly quantitative evaluation of the model-data discrepancy.

Following the 7-day time window of each reduced data point (see Section 4.3.1), we first calculate the mean of the modeled back-azimuth deviations in 7-day time intervals. Then, we calculate the monthly discrepancy using the Euclidean distances between the two sets of 7-day values (model vs. observations), building means by month (Figure 8). These values preserve the sign that corresponds to the difference between the observations and modeled back-azimuth deviations, reflecting the expected azimuthal direc-

tion of the discrepancy. Additionally, we calculate the year-long differences by averaging the magnitudes of their monthly discrepancies. These will be the final values representing the overall accuracy of each model with respect to the reduced observations (Table 1; also SI, Figures 9 to 13).

Ambrym monthly differences for 2004 (Figure 8a) oscillate between a negative maximum of $\sim -3^\circ$ to -4° around December/January for all models, and a maximum positive peak of $\sim 1.5^\circ$ around August for all but the hybrid models, which have a less-negative to maximum positive peak on April ($\sim -0.5^\circ$ and $\sim 1^\circ$ for the range-dependent and range-independent cases, respectively). The best agreement between models and observations occurs around November and March, with differences smaller than 1° . This is coincident with the times when most of the detections appear, along the “main arc sides” pointed out in Figure 2f. The negative differences in the middle of the year are clearly caused by either clutter infrasound or other volcanic sources such as Gaua/Ambae. Despite being able to predict observations produced by transient ducts (e.g., QBO/SSW), the hybrid models accumulate the highest differences during this time.

The range-dependent, hybrid model shows largest difference, with a yearly mean of $1.59 \pm 1.07^\circ$ (Table 1; also SI, Figure 9). On the other hand, the range-independent, hybrid model has the

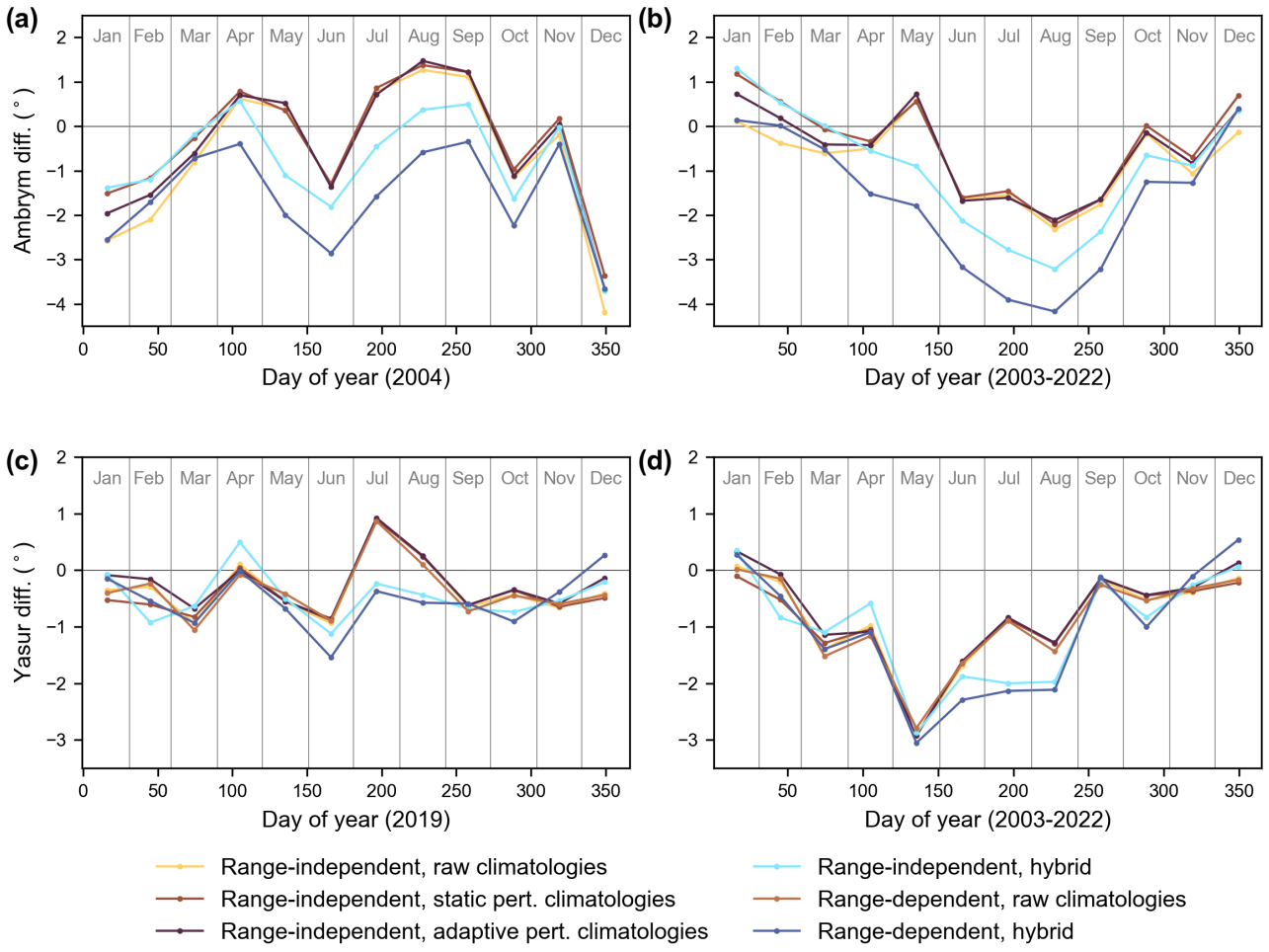


Figure 8. Euclidean distance between reduced high-frequency infrasound observations (Hupe et al. 2021) (Figures 6, 7) and interpolated modeled back-azimuths per month (non-leap year). (a) 2004 Ambrym. (b) 2003–2022 Ambrym. (c) 2019 Yasur. (d) 2003–2022 Yasur. The gray labels on top separated by vertical gray lines mark each month. (see SI, Figures 9 and 10 for more details).

smallest difference, with a yearly mean of $1.07 \pm 0.99^\circ$. Among the empirical climatology based models, the range-independent, static perturbed model follows with a $1.12 \pm 0.82^\circ$ mean difference.

The Yasur monthly differences for 2019 (Figure 8c) are mostly below 1° magnitude and negative. This is reflected in the yearly means, which have values from 0.43 to 0.58° , and spreads from ~ 0.3 to 0.4° . This shows that the models have a better agreement with the observations in this case. However, in June and July there are disagreements between the climatology-based and hybrid models that differ in sign and have the highest magnitudes, marking a period within the “capped” part of the arc hypothesized in Figure 2e. These again are discrepancies caused by periods of lower numbers of detections likely driven by clutter infrasound, or transient ducts. In this case, the hybrid models seem to correctly predict a group of detections in July that could be associated with the effects of QBO westward equatorial winds in the second half of 2019 (see Figure 5a,b), but further research is required to clarify this assertion.

The model with the smallest yearly mean difference in this case is the range-independent, adaptive perturbed climatologies ($0.43 \pm 0.29^\circ$). The range-dependent, hybrid model has the largest relative difference ($0.58 \pm 0.39^\circ$). This mismatch increase can be

mainly attributed to a peak of $\sim 1.5^\circ$ difference in June, which is an overshoot effect of the interpolation.

Overall, the considerable spread of the mean euclidean differences for both cases shows that the models, rather than better or worse in absolute terms, are comparable. This indicates that the empirical climatologies are valid to understand the specific year-long, first-order behavior of the infrasound observations for 2004 and 2019.

The comparison with the 2003–2022 stacked dataset shows an increased yearly mean difference for all models (Table 1; Figure 8b,d; also SI, Figure 10). As the multi-year comparison is suited for the empirical climatologies, the hybrid descriptions will be an upper limit reference of the monthly and year-long differences.

The monthly differences show that, when stacking the data, the overall discrepancies are negative and peak around August and May for Ambrym and Yasur cases, respectively (see Figures 8b,d). As previously shown, these negative peaks occur during periods of low numbers of candidate detections from either Ambrym or Yasur, caused by unfavorable ducting conditions, and non seasonal detections that can be associated with transient favorable ducts (QBO or SSW events) and clutter infrasound. February to April, and October to November are overall the months with smallest differences

Volcano	Year(s)	Model type	Mean diff. $\pm \sigma$ [°]
Ambrym	2004	Range-ind., raw clim.	1.38 \pm 1.08
		Range-ind., stat. pert. clim.	1.12 \pm 0.82
		Range-ind., adapt. pert. clim.	1.25 \pm 0.91
		Range-ind., hybrid	1.07 \pm 0.99
		Range-dep., raw clim.	No data
		Range-dep., hybrid	1.59 \pm 1.07
Yasur	2019	Range-ind., raw clim.	0.54 \pm 0.27
		Range-ind., stat. pert. clim.	0.56 \pm 0.24
		Range-ind., adapt. pert. clim.	0.43 \pm 0.29
		Range-ind., hybrid	0.55 \pm 0.29
		Range-dep., raw clim.	0.52 \pm 0.29
		Range-dep., hybrid	0.58 \pm 0.39
Ambrym	2003–2022	Range-ind., raw clim.	0.91 \pm 0.71
		Range-ind., stat. pert. clim.	0.91 \pm 0.67
		Range-ind., adapt. pert. clim.	0.90 \pm 0.66
		Range-ind., hybrid	1.30 \pm 1.01
		Range-dep., raw clim.	No data
		Range-dep., hybrid	1.77 \pm 1.43
Yasur	2003–2022	Range-ind., raw clim.	0.90 \pm 0.79
		Range-ind., stat. pert. clim.	0.91 \pm 0.77
		Range-ind., adapt. pert. clim.	0.86 \pm 0.79
		Range-ind., hybrid	1.08 \pm 0.86
		Range-dep., raw clim.	0.91 \pm 0.79
		Range-dep., hybrid	1.21 \pm 0.94

Table 1. Summary of mean differences with standard deviations (σ) in the considered time-window between the models and high-frequency (1–3 Hz) PMCC datasets (Hupe et al. 2021).

for Ambrym, while September to February (cyclically) are the ones for Yasur. These months align with the arc-like features pointed out in Figure 2e,f, during times of favorable ducting conditions.

Both multi-year mean differences show the same relative results (Table 1; also SI Figure 10). The range-independent, adaptive perturbed climatologies provide the minimum differences: $0.90 \pm 0.66^\circ$ for Ambrym while $0.86 \pm 0.79^\circ$ for Yasur. The range-dependent, hybrid descriptions go up to $1.77 \pm 1.43^\circ$ for Ambrym and $1.21 \pm 0.94^\circ$ for Yasur.

5 DISCUSSION

The accuracy measurements we present in Table 1 are an attempt to compare our rather simple models with a large amount of observations which have a much more complex behavior. The mean differences represent a measure of agreement between the year-long back-azimuth deviation interpolated curves and the reduced data, for a specific year (2004 or 2019) or as a multi-year stack (2003–2022). We remark that these values serve to compare between the models we tested for this specific area and the times considered, but do not provide a general interpretation of the performance of each model scheme for the globe unless future experiments show similar results. Keeping this in mind, we see that all the models perform similarly well despite the considerable differences among the used atmospheric descriptions (i.e., climatologies vs. hybrid; raw climatologies vs. perturbed climatologies) and ray tracing model types (range-independent vs. range-dependent). The mean differences remain in the range ~ 0.6 – 1.8 degrees, above IS22 nominal resolution at 1 Hz ($\sim 0.5^\circ$; Le Pichon et al. 2005a). These differences range from 0.6 to 1.2 degrees for Yasur (~ 400 km), increasing to 0.9 to 1.8 degrees for Ambrym (~ 700 km). Such a difference increase

from Yasur to Ambrym cases can be attributed to the intrinsic compounded error of ray propagation modeling with travel path length (~ 400 to ~ 700 km), and the increase in unmodelled atmospheric variability in the empirical climatologies at above mesospheric to lower thermospheric atmospheric altitudes (~ 80 – 120 km; Emmert et al. 2020), which are particularly relevant for ray-paths from Ambrym to IS22.

There is significant spread (σ) around the mean differences, representing 42–92% of each value (see Table 1). It is important to note that this value does not provide an accurate interpretation of the actual expected error, as the error distribution tends to be one-sided. To better understand the expected error in the back-azimuth deviation, the monthly curves as Figure 8 should be used, as they provide not only the magnitude but the sign of the back-azimuth deviation of the modeled infrasound in time. The variance of the candidate infrasound observations is highly influenced by overlapping non-volcanic sources (clutter) which remain present in the reduced datasets (Figures 6 and 7). Overall, these differences (~ 1 – 3°) seem to be in the same range of previous studies (Le Pichon et al. 2005a,b; Antier et al. 2007; Assink et al. 2014a, see Figure 8).

The range-independent models provide comparable or better results than the range-dependent models (Table 1). This seems counterintuitive, but it tells us that the atmospheric descriptions in the area of study only change significantly in altitude at each modeled time. Indeed, the smallest horizontal resolution is 0.25 degrees (ERA 5), or about 27 km, meaning that atmospheric changes in the order of ~ 100 km or bigger can be mapped sufficiently well. That is, for a specific day and time, localized atmospheric changes (wind speed, temperature, etc.) at this scale are not large enough to produce arrivals that are much different from the along-path mean descriptions of a representative layer (range-independent). Considering the increased computation time that range-dependent ray-tracing requires compared with range-independent ray-tracing (10 times as mentioned in the infraGA manual, Section 3.2; Blom 2014), the range-independent models are the right choice with the level of resolution and the spatiotemporal scales we pursue for modeling the azimuth deviation effects for a robust and rapid calculation scenario (e.g., a near-real-time volcano monitoring tool).

The hybrid models are the only ones able to map shorter term wind reversals that happen in the middle of the year (see Figures 6 and 7). However, the monthly means (Figure 8a,b) indicate that the hybrid models predict back-azimuths that deviate significantly from those observed. A rule of thumb to calculate year-long predictions for a specific area would be to favor climatology-based models during periods with stable seasonal ducting, while switching to NWP-based atmospheric models when events as SSW or QBO-driven wind reversals have been observed in the past. Such analysis could also benefit from the characterization of seasonal trends of stratospheric waveguides and detectability on predefined areas or station locations (e.g., Blom et al. 2023).

We note that here we use the persistent Yasur and Ambrym volcanic sources to evaluate our method on continuous data. However, this method is generally intended for sudden, unexpected, large explosive eruptions without recent priors, such as the 2011 Puyehue-Cordón Caulle eruption, Chile; or the 2015 Calbuco eruption, Chile (De Negri & Matoza 2023). For well documented, persistent, infrasound sources such as Yasur or Ambrym volcanoes, other approaches based on data regression or machine learning could better perform in terms of their predictive accuracy. However, these approaches would not be suitable for volcanic observatories without long records of prior detections and new back-azimuths,

real time atmospheric data access, and/or computational resources. That is, climatologies with ray tracing (predictions based on atmospheric structure only) are still needed to obtain critical information to characterize new transient infrasound during a volcanic emergency (De Negri & Matoza 2023).

5.1 Seasonal and daily changes of the models

Two interesting characteristics stand out at seasonal and diurnal time scales (Figures 9 and 10, for 2004 Ambrym and 2019 Yasur).

First, the asymmetry of the negative vs. positive peak seasonal back-azimuth deviations is much more marked in the empirical climatologies than the hybrid models. This peak-to-peak asymmetry seems to be driven mainly by the 12:00 UTC arrivals, especially in the climatology-based results. For Yasur volcano (southwest propagation), the empirical climatologies show deviations that have maximum values of $\sim -5^\circ / +2.5^\circ$, while the hybrid models have maximum values of $\sim -5^\circ / +5^\circ$ (Figure 9). For Ambrym volcano (south propagation), a similar asymmetry is present for the empirical climatologies, but the maximum deviation values are $\sim -7^\circ / +4^\circ$, while the hybrid models predict extremes of $\sim -5^\circ / +6^\circ$ (Figure 10). This is related to the change rate of the back-azimuth deviation from the seasonal negative peak to the positive peak (and vice-versa) which is higher for the hybrid models. On average, the rates of back-azimuth change per day on the first 100 days for the Yasur models are about $7.5/100 [^\circ/\text{day}]$ for the climatologies (Figure 9a,b,c,e right) while $10/100 [^\circ/\text{day}]$ for the hybrid models (Figure 9d,f right). For Ambrym, these values increase to about $9/100 [^\circ/\text{day}]$ for the climatologies (Figure 10a,b,c right) while $12/100 [^\circ/\text{day}]$ for the hybrid models (Figure 10d,e right). As the empirical climatologies are based on multi-year interpolated observations back to ~ 30 years (Drob et al. 2015; Emmert et al. 2020), this may possibly indicate a shift over the last three decades to higher transition rate changes between seasons. However, this is only partially supported by qualitative comparison with two specific years in the area (2004 and 2019). To better understand this behavior, further analysis should be performed by comparing a more complete set of year-long models (e.g., 2004–2020), and calculating the back-azimuth rates of the interpolated arrivals.

Second, all models present a similar semi-diurnal behavior, showing the biggest deviations at 00:00 and 12:00 UTC, and the smallest deviations at 06:00 and 18:00 UTC (e.g., days 1 to ~ 100 , and ~ 300 to 365). The change in back-azimuth deviation at distinct times of the day suggests the thermospheric duct, whose temperature is affected by the Sun's daily energy input, may have a visible influence in the total observed back-azimuth deviation. However, this semi-diurnal effect is more marked for the climatology-based than the hybrid models, suggesting that stochastic atmospheric variations could reduce the importance of this contribution. In Section 5.2 we show that there is an observable difference in number of detections during the day at least for Ambrym case (Figure 11).

The diurnal standard deviations can be above 1° in periods of strong zonal winds (westwards; day ~ 300 to 365, and 1 to ~ 80 ; Figures 9, 10 vertical bars around interpolations on right sub-figures), declining to less than 0.5° during weaker zonal wind conditions. These variations represent a secondary effect as the seasonal back-azimuth deviations can have magnitudes between ~ 5 to 7° , but could add significant differences in the back-azimuth source location for long-range propagation.

5.2 Feasibility of thermospheric arrivals

Our models use ground intercepts with turning heights at stratospheric (~ 40 km) and thermospheric (~ 110 km) altitudes (Figure 4), maximizing the number of available (near enough IS22) arrivals. But infrasound that refracts at higher altitudes (thermospheric) suffers a higher transmission loss (Sutherland & Bass 2004), and could be undetectable at the recording sensors.

Interestingly, when arranging the multi-year observations from Ambrym direction by time of day (Figure 11b,d,f,h; also SI Figure 15), we see two 6-hour time windows with larger numbers of detections centered at $\sim 07:00$ and $\sim 17:00$ UTC (18:00 and 04:00 local time, respectively). These are followed by two periods of low detections, centered at $\sim 12:00$ and $\sim 01:00$ UTC (23:00 and 12:00 local time). On the other hand, the detections from Yasur direction (Figure 11a,c,e,g; also SI Figure 15) are mostly continuous and more numerous, with one low detection time window at $\sim 01:00$ UTC. This low detection rates period has been attributed to daily increased local winds, which significantly reduce the signal-to-noise ratio at IS22 (Le Pichon et al. 2005b).

The diurnal variability is likely the effect of migrating solar tides in the mesosphere and thermosphere with dominant periods of 24, 12, and 8 hours (Le Pichon et al. 2005b). Throughout the year, the thermospheric duct turning height, mainly driven by changes in temperature, is consistently lower at 06:00 and 18:00 UTC (~ 113 – 115 km), and higher at 00:00 and 12:00 UTC (~ 117 – 121 km; see SI Figure 16). A shorter travel path (i.e., lower duct) could reduce the transmission loss by about 40 dB, allowing these waveforms to be detectable at IS22 (Le Pichon et al. 2005b; Sutherland & Bass 2004). Moreover, the infrasound propagation modeling results suggest that the bulk of detections at IS22 from the direction of Ambrym are thermospheric (Figure 4). This means their detectability would be highly influenced by periods of lower transmission loss, matching the observations.

The thermospheric duct dependence of Ambrym detections can also explain why they appear during zonal wind transition periods (equinoxes) in the multi-year stacked dataset (March–June; August–October; Figure 2f). From the ray-tracing modeling point of view, when the stratospheric duct weakens, the cross-winds reduce for North-South infrasound, making long-range infrasound propagation less sensitive to initial launching parameters. Then, the modeled rays rely on the thermospheric duct, which does not impose strong cross-winds, allowing the iterative search to find arrivals near IS22 at the cost of increased transmission losses (see Figures 2f and 5). On the other hand, the detections from Yasur are produced by East-West infrasound propagation, and will be mostly dependent on the westward stratospheric duct (January–March; November–December; Figure 7). This means that the diurnal variations will be less relevant as most of the detections are not influenced by thermospheric ducting changes.

We further investigate the transmission loss vs. time of day relation with our methodology. Using range-independent hybrid atmospheric descriptions, we calculate TL estimations for 2004 Ambrym and 2019 Yasur every 30 days at 00:00, 06:00, 12:00, and 18:00 UTC from the medians of the arrivals that fall at less than 50 km from IS22. Our results show that, as hypothesized, smaller attenuations concentrate at 06:00 and 18:00 UTC for both volcanoes (Figure 12; SI Table 2). Based on the wealth of observations at IS22 and ray-tracing simulations, there is good evidence to indicate that thermospheric arrivals from Ambrym have indeed been detected at IS22, at 06:00 and 18:00 UTC, aided by lower thermospheric duct altitudes.

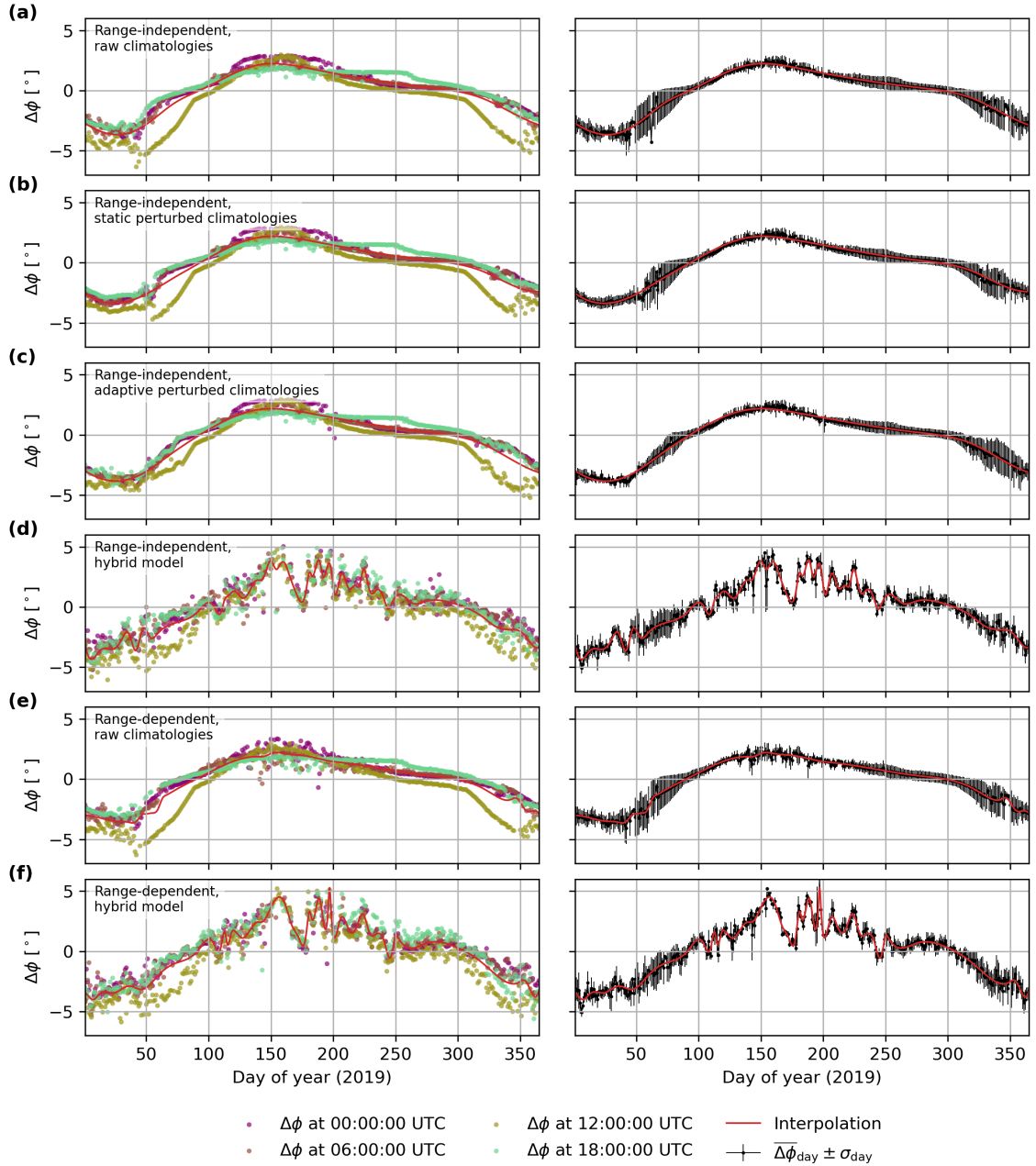


Figure 9. Comparison of back-azimuth deviation results for infrasound propagation from Yasur to IS22 during year 2019. For each 6-hour time snapshot, we plot the mean azimuth deviation of predicted arrivals falling within a distance of 5.5 km from IS22 relative to Yasur's azimuth ($\sim 43.1^\circ$). (a) to (e) Results calculated for five different model types indicated in the annotations. The calculations are performed at six-hour time-snapshots (colored points in left panels); an interpolated mean of these results is indicated by a blue line. In the right-hand panels, the interpolated mean (red line) is plotted again along with the mean daily values $\bar{\Delta\phi}_{\text{day}}$ displayed as black dots with their daily standard deviation σ_{day} indicated by a vertical thin black bar.

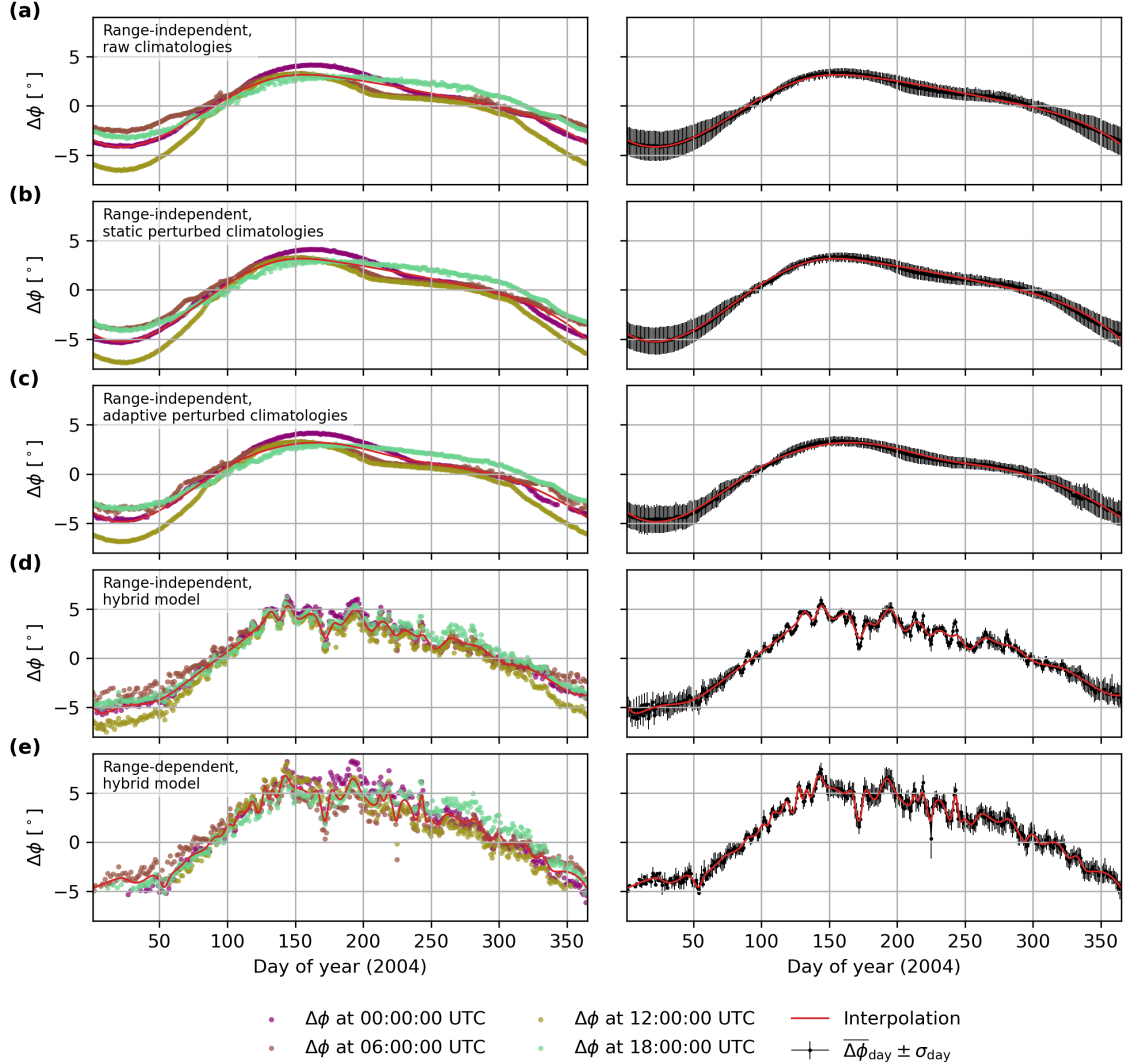


Figure 10. Similar to Figure 9, but with back-azimuth deviation results for infrasound propagation from Ambrym volcano to IS22 during 2004. In this case, the range-dependent raw-climatologies do not predict arrivals within our criteria (within 5.5 km from IS22).

6 CONCLUSIONS

We tested a methodology that aims to calculate robust, first-order estimates of long-range infrasound arrival characteristics, particularly the back-azimuth deviation, using empirical climatologies. We produced year-long models of infrasound propagation for arrivals at IMS station IS22 (Grande Terre, New Caledonia) from the Vanuatu archipelago region, including from Yasur (Tanna island, at ~ 400 km and 43°N azimuth) and Ambrym (Ambrym island, at ~ 670 km and 12°N azimuth) volcanoes.

Our goal was to investigate if the empirical climatologies were sufficient, and to what extent, to model the infrasound propagation

path effects of the atmospheric changes in altitude of the horizontal winds, temperatures, densities and pressures during a year. We chose a case where the source locations can be assumed as known and nearly-continuous, hence leaving the source mislocation and detectability effects as induced by the atmospheric variability in time. We modeled such atmospheric parameters for infrasound propagation from the ground to 150 km with empirical climatologies (HWM14/MSIS2.0), and also considered two approaches for automatically perturbing the descriptions to enhance along-path stratospheric winds. Our simplified perturbation schemes are intended to mimic the effect of gravity-wave perturbations, without

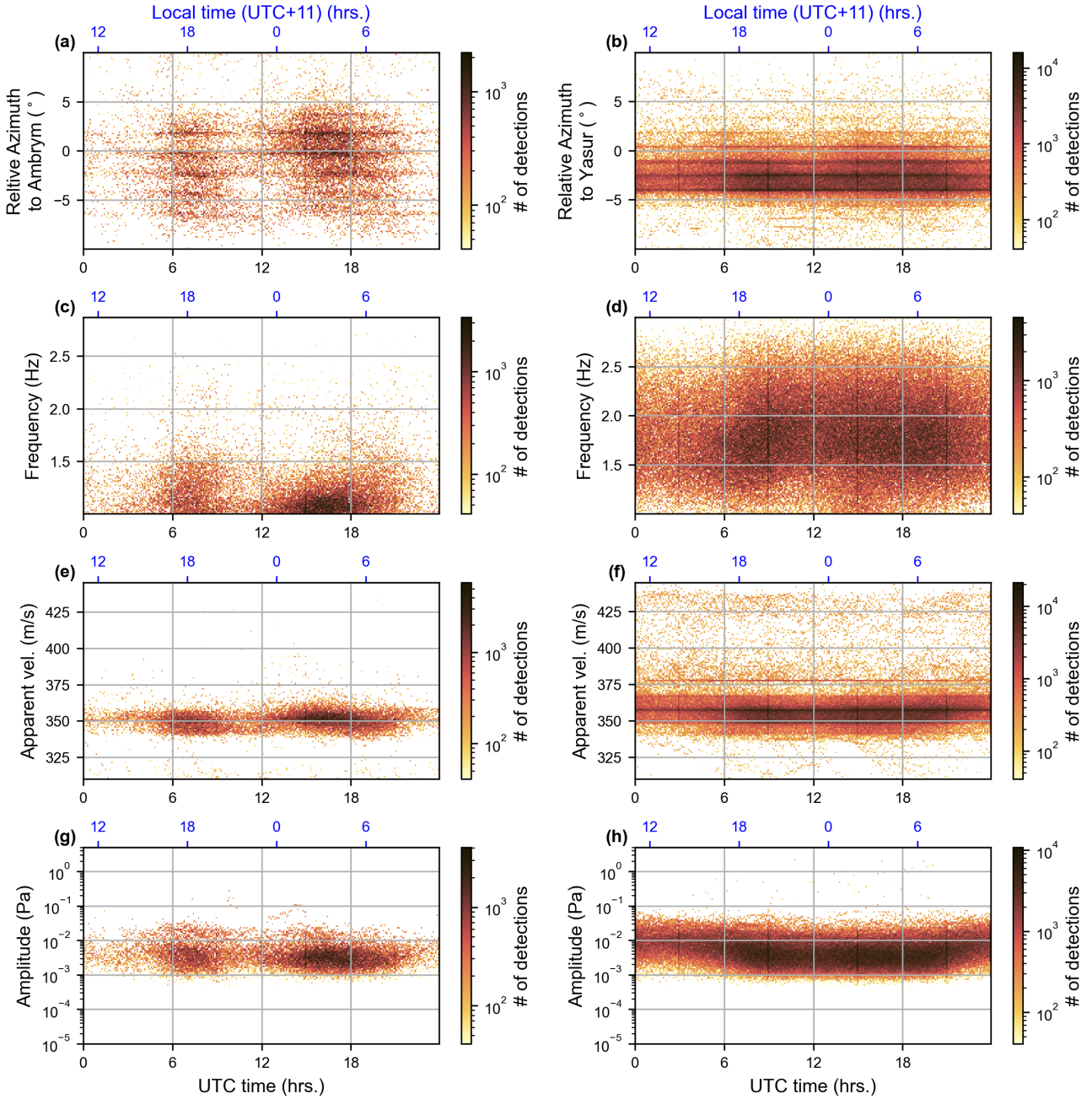


Figure 11. Example 2D histograms of detections by time of day for the 2003–2022 PMCC high-frequency (1–3 Hz) products (see also SI Figure 15). (a,c,e,g) Detections around the back-azimuth of Ambrym volcano. (b,d,f,h) Detections around the back-azimuth of Yasur volcano. (a,b) Time vs. Azimuth (deg.). (c,d) Time vs. Frequency (Hz). (e,f) Time vs. Apparent velocity (m/s). (g,h) Time vs. Amplitude (Pa).

having to resort to a full statistical ensemble treatment and thus saving computation time and simplifying the implementation.

To evaluate the accuracy and limitations of the above climatology-based approaches, we also repeated the calculations using more accurate hybrid models that merge the ERA 5 descriptions (winds and temperatures) from the ground to ~ 80 km with the climatologies for higher altitudes (> 80 km). To investigate the degree of model complexity required to match observations, we performed both range-independent and range-dependent 3D ray-tracing modeling (infraGA/geoAC (Blom & Waxler 2012)). In total, we compared six different atmospheric model parameteriza-

tions with the multi-decadal (2003 up to 2022) observations. We used the 2003–2022 open-access high-frequency (1–3 Hz) PMCC products first released by Hupe et al. (2021).

We found that the range-dependent propagation models provide comparable results to the range-independent cases, supporting the use of a simplified, layered model of the atmosphere for regional and global calculations. From July to April, all of the models depict seasonal back-azimuth changes that are generally aligned with the year-long and stacked multi-year observations. From May to June, the reversal of the zonal stratospheric winds from prevalent westward to eastward winds shows a reduction in observa-

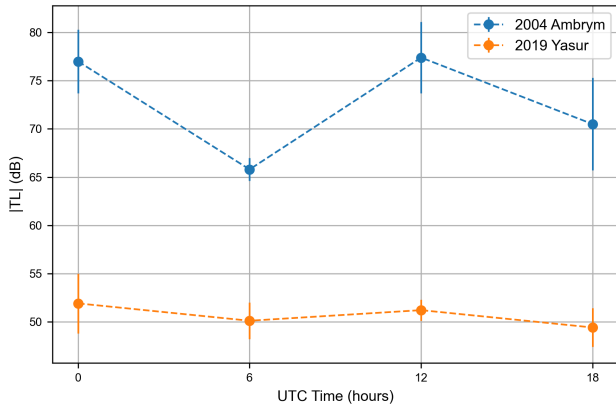


Figure 12. Transmission Loss (TL) [dB] values (medians and median absolute deviations) per year at 00:00, 06:00, 12:00 and 18:00 UTC for the cases of 2004 Ambrym and 2019 Yasur calculated with infraGA ray-tracing (1 Hz). The values in this plot are also displayed in the SI Table 2. Note that all TL values are shown as magnitudes, avoiding the negative representation (i.e., greater value means higher TL (more negative)).

tions, larger differences with the models, and only transient groups of detections likely produced by regional scale wind perturbations and transient favorable ducts (e.g., Sudden Stratospheric Warming events). The mean difference per year between the models and the high-frequency PMCC products shows that the empirical climatologies can provide comparable results with the hybrid models. The match is generally better for Yasur volcano than for Ambrym, which is likely the combined effect of increased crosswinds and propagation path lengths, plus other possible eruptive sources from similar locations such as Gaua and Ambae volcanoes complicating the attribution of detections uniquely to Ambrym. For specific years, only the hybrid models were capable of reproducing detections from transient ducts during the worst matching period (April–June). The hybrid models also better characterize the back-azimuth changes during the equinox transition periods towards the stratospheric seasonal wind reversal (around April and October).

The results from our analysis of the IS22 persistent multi-year long-range volcanic-infrasound detections indicate that empirical climatologies are useful and adequate for a rapid infrasound propagation calculation scenario (such as for a volcano monitoring system). This represents a step forward from assuming a single value of celerity and neglecting cross-winds, which has previously been assumed for rapid calculations (e.g., Matoza et al. 2017). In particular, we found that the range-independent, raw climatology models are well-suited to obtain robust first-order estimates of arrival back-azimuths for large-scale, year-long infrasound propagation in this region. However, the climatologies do not perform as well as the hybrid models when the stratospheric duct weakens (equinoxes) or when short-term (days) wind reversals allow favorable ducts to appear during upwind conditions (summer). In such cases, a more accurate model with hybrid descriptions should be performed at a later time, given more time to download the specifications and run the simulations. We also emphasize that propagation models based on climatologies can be pre-computed, since climatologies do not use any current atmospheric data. Pre-computation of infrasound propagation paths using climatologies could be useful for near-real-time infrasound monitoring applications such as in volcano-monitoring systems (De Negri & Matoza 2023).

Our proposed adaptive perturbation of the empirical clima-

tologies, which is intended as a simplified alternative to a full gravity-wave realization approach (ensemble averaging), was successful at enhancing stratospheric predictions. This approach may also be convenient for a rapid scenario where only an approximation of expected backazimuth deviations is needed. As stratospheric gravity waves are known to considerably reduce infrasound transmission losses (i.e., enhance propagation and ducting conditions; Listowski et al. 2024), future enhancements to the adaptive approach could be explored.

Finally, we remark that none of the atmospheric models we considered, including the hybrid specifications, fully explain all of the observations (e.g., more negative deviations on the first \sim 50 days of 2004 for Ambrym, and \sim 250–350 of 2019 for Yasur on Figure 6). Thus, our study supports the notion that continuous infrasound observations can be used to verify and potentially improve atmospheric specifications (e.g., Le Pichon et al. 2005b; Antier et al. 2007; Assink et al. 2014a; Vorobeva et al. 2023). To better resolve middle atmospheric dynamics in the mesospheric to lower thermospheric altitude range, other Numerical Weather Prediction models could be used in place of the hybrid approach we implemented, such as the Whole Atmosphere Community Climate Model with thermosphere and ionosphere extension (WACCM-X; Liu et al. 2018) which is nudged with the Modern-Era Retrospective analysis for Research and Applications (MERRA-2; e.g., Vorobeva et al. 2023). However, this is beyond the aim of this study, as our goal was to assess a simplified low-computational cost methodology for first-order estimates.

This work focuses on volcanic infrasound detections at one station in the International Monitoring System. Generalizing these results will be important, both for other volcano-to-array paths globally and for other monitoring applications (e.g., global nuclear test monitoring), as mislocations due to unmodelled backazimuth deviations are a global issue. We suggest that additional long-range studies using other persistent volcanic source locations with large available detection records (e.g., Etna volcano) could be a step forward in this direction, further evaluating the applicability of this method beyond volcanic infrasound source location in near-real time. Additionally, considering other persistent anthropogenic or natural infrasound sources with large historical sets of detections (e.g., microbaroms, dams, etc.) could serve to understand to what extent this methodology could be applied to other infrasound generating phenomena.

ACKNOWLEDGMENTS

This work was funded by NSF Grant EAR-1847736. R.S.D. thanks C. Scanlon for reviewing and improving the manuscript. All authors thank the CTBTO and the IMS station operators for guaranteeing the high quality of the infrasound data. The views expressed herein are those of the authors and do not necessarily reflect the views of the CTBTO Preparatory Commission. We also wish to thank Dr. David Green and Dr. Stephen Arrowsmith for their reviews, which helped us to improve the manuscript.

Data Availability

All International Monitoring System data are available for scientific studies through the CTBTO vDEC platform (<https://www.ctbto.org/specials/vdec/>). The PMCC products used in this study can be accessed through the Geoportal

of the Federal Institute for Geosciences and Natural Resources (BGR, Germany; <https://geoportal.bgr.de>) (see Hupe et al. 2022). For the hybrid models we used the CDS API tools freely provided by European Centre for Medium-Range Weather Forecasts (ECMWF) to obtain the necessary ERA5 reanalysis profiles, publicly available for academic research (<https://confluence.ecmwf.int/display/CKB/How+to+download+ERA5>). The climatology (HWM/MSISE) model codes are available from Drob et al. (2015) and Emmert et al. (2020), respectively. The 3D ray-tracing infrasound propagation algorithms are available for research purposes from the Los Alamos National Laboratory (LANL, USA) GitHub repository (<https://github.com/LANL-Seismoacoustics/infraGA>). The main code used in this project (ARCADE), is available for research purposes in the GitHub repository (<https://github.com/rodrum/arcade>) along with instructions and examples. The last stable code release can be accessed in Zenodo in <https://doi.org/10.5281/zenodo.13383432> (De Negri 2024).

REFERENCES

Anstey, J. A. & Shepherd, T. G., 2014. High-latitude influence of the quasi-biennial oscillation, *Quarterly Journal of the Royal Meteorological Society*, **140**(678), 1–21.

Antier, K., Le Pichon, A., Vergniolle, S., Zielinski, C., & Lardy, M., 2007. Multiyear validation of the NRL-G2S wind fields using infrasound from Yasur, *Journal of Geophysical Research: Atmospheres*, **112**(D23), eprint: <https://onlinelibrary.wiley.com/doi/pdf/10.1029/2007JD008462>.

Arrowsmith, S. J., Whitaker, R., Taylor, S. R., Burlacu, R., Stump, B., Hedlin, M., Randall, G., Hayward, C., & Revelle, D., 2008. Regional monitoring of infrasound events using multiple arrays: application to Utah and Washington State, *Geophys. J. Int.*, **175**, 291–300, ISBN: 175/1/291/718295.

Assink, J. D., Pichon, A. L., Blanc, E., Kallel, M., & Khemiri, L., 2014a. Evaluation of wind and temperature profiles from ECMWF analysis on two hemispheres using volcanic infrasound, *Journal of Geophysical Research: Atmospheres*, **119**(14), 8659–8683, eprint: <https://onlinelibrary.wiley.com/doi/pdf/10.1002/2014JD021632>.

Assink, J. D., Waxler, R., Smets, P., & Evers, L. G., 2014b. Bidirectional infrasonic ducts associated with sudden stratospheric warming events, *Journal of Geophysical Research: Atmospheres*, **119**(3), 1140–1153.

Bani, P., Boudon, G., Balcone-Boissard, H., Delmelle, P., Quiniou, T., Lefèvre, J., Bule, E. G., Hiroshi, S., & Lardy, M., 2016. The 2009–2010 eruption of Gaua volcano (Vanuatu archipelago): Eruptive dynamics and unsuspected strong halogens source, *Journal of Volcanology and Geothermal Research*, **322**, 63–75.

Beaumais, A., Bertrand, H., Chazot, G., Dosso, L., & Robin, C., 2016. Temporal magma source changes at Gaua volcano, Vanuatu island arc, *Journal of Volcanology and Geothermal Research*, **322**, 30–47.

Bell, B., Hersbach, H., Simmons, A., Berrisford, P., Dahlgren, P., Horányi, A., Muñoz-Sabater, J., Nicolas, J., Radu, R., Schepers, D., Soci, C., Villaume, S., Bidlot, J., Haimberger, L., Woollen, J., Buontempo, C., & Thépaut, J., 2021. The ERA5 global reanalysis: Preliminary extension to 1950, *Quarterly Journal of the Royal Meteorological Society*, **147**(741), 4186–4227.

Blom, P., 2020. The influence of irregular terrain on infrasonic propagation in the troposphere, *The Journal of the Acoustical Society of America*, **148**(4), 1984–1997, Publisher: Acoustical Society of America.

Blom, P. & Waxler, R., 2012. Impulse propagation in the nocturnal boundary layer: Analysis of the geometric component, *The Journal of the Acoustical Society of America*, **131**(5), 3680–3690, Publisher: Acoustical Society of America.

Blom, P. & Waxler, R., 2017. Modeling and observations of an elevated, moving infrasonic source: Eigenray methods, *The Journal of the Acoustical Society of America*, **141**(4), 2681–2692.

Blom, P., Waxler, R., & Frazier, G., 2023. Quantification of spatial and seasonal trends in the atmosphere and construction of statistical models for infrasonic propagation, *Geophysical Journal International*, **235**(2), 1007–1020.

Blom, P. S., 2014. infraGA/GeoAc: Numerical tools to model infrasonic propagation in the limit of geometric acoustics, <https://github.com/LANL-Seismoacoustics/infraGA/blob/master/doc/tex-old/manual.pdf>.

Campus, P. & Christie, D. R., 2009. Worldwide Observations of Infrasonic Waves, in *Infrasound Monitoring for Atmospheric Studies*, pp. 185–234, eds Le Pichon, A., Blanc, E., & Hauchecorne, A., Springer Netherlands, Dordrecht.

Cansi, Y., 1995. An automatic seismic event processing for detection and location: The P.M.C.C. Method, *Geophysical Research Letters*, **22**(9), 1021–1024.

Cansi, Y. & Klinger, Y., 1997. An automated data processing method for mini-arrays, *Newsletter of the European-Mediterranean Seismological Center*, **11**, 2–4.

Caudron, C., Taisne, B., Garcés, M., Alexis, L. P., & Mialle, P., 2015. On the use of remote infrasound and seismic stations to constrain the eruptive sequence and intensity for the 2014 Kelud eruption, *Geophysical Research Letters*, **42**(16), 6614–6621, Publisher: Blackwell Publishing Ltd.

Ceranna, L., Matoza, R., Hupe, P., Le Pichon, A., & Landès, M., 2019. Systematic Array Processing of a Decade of Global IMS Infrasound Data, in *Infrasound Monitoring for Atmospheric Studies*, pp. 471–482, eds Le Pichon, A., Blanc, E., & Hauchecorne, A., Springer International Publishing, Cham.

Christie, D. R. & Campus, P., 2010. The IMS Infrasound Network: Design and Establishment of Infrasound Stations, in *Infrasound Monitoring for Atmospheric Studies*, pp. 29–75, eds Le Pichon, A., Blanc, E., & Hauchecorne, A., Springer Netherlands, Dordrecht.

Coppola, D., Laiolo, M., & Cigolini, C., 2016. Fifteen years of thermal activity at Vanuatu's volcanoes (2000–2015) revealed by MIROVA, *Journal of Volcanology and Geothermal Research*, **322**, 6–19.

Dabrowa, A., Green, D., Rust, A., & Phillips, J., 2011. A global study of volcanic infrasound characteristics and the potential for long-range monitoring, *Earth and Planetary Science Letters*, **310**(3–4), 369–379.

De Angelis, S., Fee, D., Haney, M., & Schneider, D., 2012. Detecting hidden volcanic explosions from Mt. Cleveland Volcano, Alaska with infrasound and ground-coupled airwaves, *Geophysical Research Letters*, **39**(21), eprint: <https://onlinelibrary.wiley.com/doi/pdf/10.1029/2012GL053635>.

De Negri, R., 2024. rodrum/arcade: ARCADE release v1.1.

De Negri, R. & Matoza, R. S., 2023. Rapid Location of Remote Volcanic Infrasound Using 3D Ray Tracing and Empirical Climatologies: Application to the 2011 Cordón Caulle and 2015 Calbuco Eruptions, Chile, *Journal of Geophysical Research: Solid Earth*, **128**(3), e2022JB025735, eprint: <https://onlinelibrary.wiley.com/doi/pdf/10.1029/2022JB025735>.

De Negri, R. S., Rose, K. M., Matoza, R. S., Hupe, P., & Ceranna, L., 2022. Long-Range Multi-Year Infrasonic Detection of Eruptive Activity at Mount Michael Volcano, South Sandwich Islands, *Geophysical Research Letters*, **49**(7).

Dierckx, P., 1995. *Curve and Surface Fitting with Splines*, Clarendon Press.

Drob, D., 2019. Meteorology, Climatology, and Upper Atmospheric Composition for Infrasound Propagation Modeling, in *Infrasound Monitoring for Atmospheric Studies: Challenges in Middle Atmosphere Dynamics and Societal Benefits*, pp. 485–508, eds Le Pichon, A., Blanc, E., & Hauchecorne, A., Springer International Publishing, Cham.

Drob, D. P., Picone, J. M., Garcés, M., & Garce, M., 2003. Global morphology of infrasound propagation, *Journal of Geophysical Research*, **108**(D21), 1–12, Publisher: Wiley-Blackwell.

Drob, D. P., Garcés, M., Hedlin, M., & Brachet, N., 2010. The Temporal Morphology of Infrasound Propagation, *Pure and Applied Geophysics*, **167**(4–5), 437–453, Publisher: Birkhäuser-Verlag.

Drob, D. P., Broutman, D., Hedlin, M. A., Winslow, N. W., & Gibson, R. G., 2013. A method for specifying atmospheric gravity wavefields for

long-range infrasound propagation calculations, *Journal of Geophysical Research Atmospheres*, **118**(10), 3933–3943.

Drob, D. P., Emmert, J. T., Meriwether, J. W., Makela, J. J., Doornbos, E., Conde, M., Hernandez, G., Noto, J., Zawdie, K. A., McDonald, S. E., Huba, J. D., & Klenzing, J. H., 2015. An update to the Horizontal Wind Model (HWM): The quiet time thermosphere, *Earth and Space Science*, **2**(7), 301–319.

Eissen, J.-P., Lefevre, C., Maillet, P., Morvan, G., & Nohara, M., 1991. Petrology and geochemistry of the central North Fiji Basin spreading centre (Southwest Pacific) between 16°S and 22°S, *Marine Geology*, **98**(2), 201–239.

Emmert, J. T., Drob, D. P., Picone, J. M., Siskind, D. E., Jones Jr., M., Mlynczak, M. G., Bernath, P. F., Chu, X., Doornbos, E., Funke, B., Goncharenko, L. P., Hervig, M. E., Schwartz, M. J., Sheese, P. E., Vargas, F., Williams, B. P., & Yuan, T., 2020. NRLMSIS 2.0: A Whole-Atmosphere Empirical Model of Temperature and Neutral Species Densities, *Earth and Space Science*, **8**(3), e2020EA001321, [eprint: https://onlinelibrary.wiley.com/doi/pdf/10.1029/2020EA001321](https://onlinelibrary.wiley.com/doi/pdf/10.1029/2020EA001321).

Evers, L. & Haak, H., 2005. The detectability of infrasound in The Netherlands from the Italian volcano Mt. Etna, *Journal of Atmospheric and Solar-Terrestrial Physics*, **67**(3), 259–268.

Fee, D., Garces, M., & Steffke, A., 2010. Infrasound from Tungurahua Volcano 2006–2008: Strombolian to Plinian eruptive activity, *Journal of Volcanology and Geothermal Research*, **193**(1–2), 67–81.

Garcés, M., Fee, D., Steffke, A., McCormack, D., Servranckx, R., Bass, H., Hetzer, C., Hedlin, M., Matoza, R., Yepes, H., & Ramon, P., 2008. Capturing the acoustic fingerprint of stratospheric ash injection, *Eos*, **89**(40), 377–378, ISBN: 0096-3941.

Garcés, M. A., Hansen, R. A., & Lindquist, K. G., 1998. Traveltimes for infrasonic waves propagating in a stratified atmosphere, *Geophysical Journal International*, **135**(1), 255–263, Publisher: Oxford University Press.

Gheri, D., Marchetti, E., Belli, G., Pichon, A. L., Boulenger, V., Hupe, P., Ceranna, L., Mialle, P., & Hereil, P., 2023. Monitoring of Indonesian volcanoes with the ISO6 infrasound array, *Journal of Volcanology and Geothermal Research*, **434**, 107753.

Green, D. N. & Bowers, D., 2010. Estimating the detection capability of the International Monitoring System infrasound network, *Journal of Geophysical Research*, **115**(D18), D18116.

Green, D. N., Vergoz, J., Gibson, R., Pichon, A. L., & Ceranna, L., 2011. Infrasound radiated by the gerdec and chelopechene explosions : propagation along unexpected paths, *Geophysical Journal International*, pp. 890–910.

Green, D. N., Matoza, R. S., Vergoz, J., & Le Pichon, A., 2012. Infrasonic propagation from the 2010 Eyjafjallajökull eruption: Investigating the influence of stratospheric solar tides, *Journal of Geophysical Research: Atmospheres*, **117**(D21), D21202.

Green, D. N., Evers, L. G., Fee, D., Matoza, R. S., Snellen, M., Smets, P., & Simons, D., 2013. Hydroacoustic, infrasonic and seismic monitoring of the submarine eruptive activity and sub-aerial plume generation at South Sarigan, May 2010, *Journal of Volcanology and Geothermal Research*, **257**, 31–43.

Hedlin, M. A. H., Garces, M., Bass, H., Hayward, C., Herrin, G., Olson, J., & Wilson, C., 2002. Listening to the secret sounds of Earth's atmosphere, *Eos, Transactions American Geophysical Union*, **83**(48), 557–565, [eprint: https://onlinelibrary.wiley.com/doi/pdf/10.1029/2002EO000383](https://onlinelibrary.wiley.com/doi/pdf/10.1029/2002EO000383).

Hupe, P., Ceranna, L., Le Pichon, A., Matoza, R. S., & Mialle, P., 2021. Higher frequency data products of the International Monitoring System's infrasound stations [NetCDF].

Hupe, P., Ceranna, L., Le Pichon, A., Matoza, R. S., & Mialle, P., 2022. International monitoring system infrasound data products for atmospheric studies and civilian applications, *Earth System Science Data*, **14**, 4201–4230.

Jones, R. M., 1986. HARPA Manual.

Kidston, J., Scaife, A. A., Hardiman, S. C., Mitchell, D. M., Butchart, N., Baldwin, M. P., & Gray, L. J., 2015. Stratospheric influence on tropospheric jet streams, storm tracks and surface weather, *Nature Geoscience*, **8**(6), 433–440, Publisher: Nature Publishing Group.

Lalande, J.-M., Sèbe, O., Landès, M., Blanc-Benon, P., Matoza, R. S., Le Pichon, A., & Blanc, E., 2012. Infrasound data inversion for atmospheric sounding, *Geophysical Journal International*, **190**(1), 687–701.

Le Pichon, A., Blanc, E., & Drob, D., 2005a. Probing high-altitude winds using infrasound, *Journal of Geophysical Research*, **110**(D20), D20104.

Le Pichon, A., Blanc, E., Drob, D., Lambotte, S., Dessa, J. X., Lardy, M., Bani, P., & Vergniolle, S., 2005b. Infrasound monitoring of volcanoes to probe high-altitude winds, *Journal of Geophysical Research Atmospheres*, **110**(13), 1–12.

Le Pichon, A., Blanc, E., Drob, D., Lambotte, S., Dessa, J. X., Lardy, M., Bani, P., & Vergniolle, S., 2005c. Infrasound monitoring of volcanoes to probe high-altitude winds, *Journal of Geophysical Research Atmospheres*, **110**(13), 1–12.

Le Pichon, A., Antier, K., & Drob, D., 2006. Multiyear validation of the NRL-G2S wind fields using infrasound from Yasur, *InfraMatics*, (16), 1–9.

Le Pichon, A., Vergoz, J., Blanc, E., Guibert, J., Ceranna, L., Evers, L., & Brachet, N., 2009a. Assessing the performance of the International Monitoring System's infrasound network: Geographical coverage and temporal variabilities, *Journal of Geophysical Research*, **114**(D8), D08112.

Le Pichon, A., Vergoz, J., Cansi, Y., Ceranna, L., & Drob, D., 2009b. Contribution of Infrasound Monitoring for Atmospheric Remote Sensing, in *Infrasound Monitoring for Atmospheric Studies*, pp. 629–646, eds Le Pichon, A., Blanc, E., & Hauchecorne, A., Springer Netherlands, Dordrecht.

Le Pichon, A., Matoza, R. S., Brachet, N., & Cansi, Y., 2010. Recent Enhancements of the PMCC Infrasound Signal Detector, *InfraMatics*, (26), 1–8.

Listowski, C., Stephan, C. C., Le Pichon, A., Hauchecorne, A., Kim, Y.-H., Achatz, U., & Bölöni, G., 2024. Stratospheric Gravity Waves Impact on Infrasound Transmission Losses Across the International Monitoring System, *Pure and Applied Geophysics*.

Liu, H.-L., Bardeen, C. G., Foster, B. T., Lauritzen, P., Liu, J., Lu, G., Marsh, D. R., Maute, A., McInerney, J. M., Pedatella, N. M., Qian, L., Richmond, A. D., Roble, R. G., Solomon, S. C., Vitt, F. M., & Wang, W., 2018. Development and Validation of the Whole Atmosphere Community Climate Model With Thermosphere and Ionosphere Extension (WACCM-X 2.0), *Journal of Advances in Modeling Earth Systems*, **10**(2), 381–402, [eprint: https://onlinelibrary.wiley.com/doi/pdf/10.1002/2017MS001232](https://onlinelibrary.wiley.com/doi/pdf/10.1002/2017MS001232).

Maher, S. P., Matoza, R. S., Jolly, A., de Groot-Hedlin, C., Gee, K. L., Fee, D., & Iezzi, A. M., 2022. Evidence for near-source nonlinear propagation of volcano infrasound from Strombolian explosions at Yasur Volcano, Vanuatu, *Bulletin of Volcanology*, **84**(4), 41.

Marchetti, E., Ripepe, M., Delle Donne, D., Genco, R., Finizola, A., & Garaebiti, E., 2013. Blast waves from violent explosive activity at Yasur Volcano, Vanuatu, *Geophysical Research Letters*, **40**(22), 5838–5843, [eprint: https://onlinelibrary.wiley.com/doi/pdf/10.1002/2013GL057900](https://onlinelibrary.wiley.com/doi/pdf/10.1002/2013GL057900).

Marchetti, E., Ripepe, M., Campus, P., Le Pichon, A., Vergoz, J., Lacanna, G., Mialle, P., Héreil, P., & Husson, P., 2019. Long range infrasound monitoring of Etna volcano, *Scientific reports*, **9**(1), 18015.

Marcillo, O., Johnson, J. B., & Hart, D., 2012. Implementation, Characterization, and Evaluation of an Inexpensive Low-Power Low-Noise Infrasound Sensor Based on a Micromachined Differential Pressure Transducer and a Mechanical Filter, *Journal of Atmospheric and Oceanic Technology*, **29**(9), 1275–1284, Publisher: American Meteorological Society Section: Journal of Atmospheric and Oceanic Technology.

Marty, J., 2019. The IMS Infrasound Network: Current Status and Technological Developments, in *Infrasound Monitoring for Atmospheric Studies: Challenges in Middle Atmosphere Dynamics and Societal Benefits*, pp. 3–62, eds Le Pichon, A., Blanc, E., & Hauchecorne, A., Springer International Publishing, Cham.

Matoza, R., Fee, D., Green, D., & Mialle, P., 2019. Volcano Infrasound and the International Monitoring System, in *Infrasound Monitoring for Atmospheric Studies*, pp. 1023–1077, eds Le Pichon, A., Blanc, E., & Hauchecorne, A., Springer International Publishing, Cham.

Matoza, R. S., Hedlin, M. A. H., & Garcés, M. A., 2007. An infrasound array study of Mount St. Helens, *Journal of Volcanology and Geothermal Research*, **160**(3-4), 249–262, ISBN: 0377-0273.

Matoza, R. S., Le Pichon, A., Vergoz, J., Herry, P., Lalande, J.-M., Lee, H.-i., Che, I.-Y., & Rybin, A., 2011a. Infrasonic observations of the June 2009 Sarychev Peak eruption, Kuril Islands: Implications for infrasonic monitoring of remote explosive volcanism, *Journal of Volcanology and Geothermal Research*, **200**(1), 35–48.

Matoza, R. S., Vergoz, J., Le Pichon, A., Ceranna, L., Green, D. N., Evers, L. G., Ripepe, M., Campus, P., Liszka, L., Kvaerna, T., Kjartansson, E., & Höskulsson, A., 2011b. Long-range acoustic observations of the Eyjafjallajökull eruption, Iceland, April–May 2010, *Geophysical Research Letters*, **38**(6), 1–5, ISBN: 0094-8276.

Matoza, R. S., Landès, M., Le Pichon, A., Ceranna, L., & Brown, D., 2013. Coherent ambient infrasound recorded by the International Monitoring System: COHERENT AMBIENT INFRASOUND, *Geophysical Research Letters*, **40**(2), 429–433.

Matoza, R. S., Green, D. N., Le Pichon, A., Shearer, P. M., Fee, D., Mialle, P., & Ceranna, L., 2017. Automated detection and cataloging of global explosive volcanism using the International Monitoring System infrasound network, *Journal of Geophysical Research: Solid Earth*, **122**(4), 2946–2971.

Matoza, R. S., Fee, D., Green, D. N., Le Pichon, A., Vergoz, J., Haney, M. M., Mikesell, T. D., Franco, L., Valderrama, O. A., Kelley, M. R., McKee, K., & Ceranna, L., 2018. Local, Regional, and Remote Seismo-acoustic Observations of the April 2015 VEI 4 Eruption of Calbuco Volcano, Chile, *Journal of Geophysical Research: Solid Earth*, **123**(5), 3814–3827, Publisher: Wiley-Blackwell.

Matoza, R. S., Chouet, B. A., Jolly, A. D., Dawson, P. B., Fitzgerald, R. H., Kennedy, B. M., Fee, D., Iezzi, A. M., Kilgour, G. N., Garaebiti, E., & Cevard, S., 2022a. High-rate very-long-period seismicity at Yasur volcano, Vanuatu: source mechanism and decoupling from surficial explosions and infrasound, *Geophysical Journal International*, **230**(1), 392–426.

Matoza, R. S., Fee, D., Assink, J. D., Iezzi, A. M., Green, D. N., Kim, K., Toney, L., Lecocq, T., Krishnamoorthy, S., Lalande, J.-M., Nishida, K., Gee, K. L., Haney, M. M., Ortiz, H. D., Brissaud, Q., Martire, L., Rolland, L., Vergados, P., Nippes, A., Park, J., Shani-Kadmiel, S., Witsil, A., Arrowsmith, S., Caudron, C., Watada, S., Perttu, A. B., Taisne, B., Mialle, P., Le Pichon, A., Vergoz, J., Hupe, P., Blom, P. S., Waxler, R., De Angelis, S., Snively, J. B., Ringler, A. T., Anthony, R. E., Jolly, A. D., Kilgour, G., Averbuch, G., Ripepe, M., Ichihara, M., Arciniega-Ceballos, A., Astafyeva, E., Ceranna, L., Cevard, S., Che, I.-Y., De Negri, R., Ebeling, C. W., Evers, L. G., Franco-Marin, L. E., Gabrielson, T. B., Hafner, K., Harrison, R. G., Komjathy, A., Lacanna, G., Lyons, J., Macpherson, K. A., Marchetti, E., McKee, K. F., Mellors, R. J., Mendo-Pérez, G., Mikesell, T. D., Munaibari, E., Oyola-Merced, M., Park, I., Pilger, C., Ramos, C., Ruiz, M. C., Sabatini, R., Schwaiger, H. F., Tailpied, D., Talmadge, C., Vidot, J., Webster, J., & Wilson, D. C., 2022b. Atmospheric waves and global seismoacoustic observations of the January 2022 Hunga eruption, Tonga, *Science*, **377**(6601), 95–100, Publisher: American Association for the Advancement of Science.

McKee, K., Smith, C. M., Reath, K., Snee, E., Maher, S., Matoza, R. S., Carn, S., Mastin, L., Anderson, K., Damby, D., Roman, D. C., Degtereov, A., Rybin, A., Chibisova, M., Assink, J. D., de Negri Leiva, R., & Perttu, A., 2021a. Evaluating the state-of-the-art in remote volcanic eruption characterization part I: Raikoke volcano, kuril islands, *Journal of Volcanology and Geothermal Research*, **419**, 107354.

McKee, K., Smith, C. M., Reath, K., Snee, E., Maher, S., Matoza, R. S., Carn, S., Roman, D. C., Mastin, L., Anderson, K., Damby, D., Itikarai, I., Mulina, K., Saunders, S., Assink, J. D., de Negri Leiva, R., & Perttu, A., 2021b. Evaluating the state-of-the-art in remote volcanic eruption characterization part II: Ulawun volcano, papua new guinea, *Journal of Volcanology and Geothermal Research*, **420**, 107381.

Meier, K., Hort, M., Wassermann, J., & Garaebiti, E., 2016. Strombolian surface activity regimes at Yasur volcano, Vanuatu, as observed by Doppler radar, infrared camera and infrasound, *Journal of Volcanology and Geothermal Research*, **322**, 184–195.

Modrak, R. T., Arrowsmith, S. J., & Anderson, D. N., 2010. A Bayesian framework for infrasound location, *Geophysical Journal International*, **181**(1), 399–405, Publisher: Oxford Academic.

Morelli, R. S., Gheri, D., Campus, P., Coppola, D., & Marchetti, E., 2022. Long range infrasound monitoring of Yasur volcano, *Journal of Volcanology and Geothermal Research*, **432**, 107707.

Morton, E. A. & Arrowsmith, S. J., 2014. The Development of Global Probabilistic Propagation Look-Up Tables for Infrasound Celerity and Back-Azimuth Deviation, *Seismological Research Letters*, **85**(6), 1223–1233, Publisher: GeoScienceWorld.

Ortiz, H. D., Matoza, R. S., Garapati, C., Rose, K., Ramón, P., & Ruiz, M. C., 2020. Multi-year regional infrasound detection of Tungurahua, El Reventador, and Sangay volcanoes in Ecuador from 2006 to 2013, *Proceedings of Meetings on Acoustics*, **41**(1), 022003.

Park, I., Jolly, A., Matoza, R. S., Kennedy, B., Kilgour, G., Johnson, R., Garaebiti, E., & Cevard, S., 2021. Seismo-acoustic characterisation of the 2018 Ambae (Manaro Voui) eruption, Vanuatu, *Bulletin of Volcanology*, **83**(9), 60.

Perttu, A., Taisne, B., De Angelis, S., Assink, J. D., Tailpied, D., & Williams, R. A., 2020. Estimates of plume height from infrasound for regional volcano monitoring, *Journal of Volcanology and Geothermal Research*, **402**, 106997.

Schwaiger, H. F., Iezzi, A. M., & Fee, D., 2019. AVO-G2S: A modified, open-source Ground-to-Space atmospheric specification for infrasound modeling, *Computers and Geosciences*, **125**, 90–97.

Simkin, T. & Siebert, L., 1994. *Volcanoes of the world: a regional directory, gazetteer, and chronology of volcanism during the last 10,000 years*, Geoscience Press, Tucson, Ariz, 2nd edn.

Smets, P. S. M., Evers, L. G., Näsholm, S. P., & Gibbons, S. J., 2014. Probabilistic infrasound propagation using realistic atmospheric perturbations, *Geophysical Research Letters*, **42**(15), 6510–6517, Publisher: Blackwell Publishing Ltd.

Smets, P. S. M., Assink, J. D., Le Pichon, A., & Evers, L. G., 2016. ECMWF SSW forecast evaluation using infrasound, *Journal of Geophysical Research: Atmospheres*, **121**(9), 4637–4650, Publisher: Wiley-Blackwell.

Spina, L., Taddeucci, J., Cannata, A., Gresta, S., Lodato, L., Privitera, E., Scarlato, P., Gaeta, M., Gaudin, D., & Palladino, D. M., 2016. "Explosive volcanic activity at Mt. Yasur: A characterization of the acoustic events (9–12th July 2011)", *Journal of Volcanology and Geothermal Research*, **322**, 175–183.

Sutherland, L. C. & Bass, H. E., 2004. Atmospheric absorption in the atmosphere up to 160 km, *The Journal of the Acoustical Society of America*, **115**(3), 1012–1032.

Tailpied, D., Le Pichon, A., Marchetti, E., Assink, J., & Vergniolle, S., 2017. Assessing and optimizing the performance of infrasound networks to monitor volcanic eruptions, *Geophysical Journal International*, **208**(1), 437–448.

Taisne, B., Perttu, A., Tailpied, D., Caudron, C., & Simonini, L., 2019. Atmospheric Controls on Ground- and Space-Based Remote Detection of Volcanic Ash Injection into the Atmosphere, and Link to Early Warning Systems for Aviation Hazard Mitigation, in *Infrasound Monitoring for Atmospheric Studies*, pp. 1079–1105, eds Le Pichon, A., Blanc, E., & Hauchecorne, A., Springer International Publishing, Cham.

Vergniolle, S. & Métrich, N., 2016. A bird's eye view of "Understanding volcanoes in the Vanuatu arc", *Journal of Volcanology and Geothermal Research*, **322**, 1–5.

Vergoz, J., Hupe, P., Listowski, C., Le Pichon, A., Garcés, M., Marchetti, E., Labazuy, P., Ceranna, L., Pilger, C., Gaebler, P., Näsholm, S., Brissaud, Q., Poli, P., Shapiro, N., De Negri, R., & Mialle, P., 2022. IMS observations of infrasound and acoustic-gravity waves produced by the January 2022 volcanic eruption of Hunga, Tonga: A global analysis, *Earth and Planetary Science Letters*, **591**, 117639.

Vorobeva, E., Assink, J., Espy, P. J., Renkwick, T., Chunchuzov, I., & Näsholm, S. P., 2023. Probing Gravity Waves in the Middle Atmosphere Using Infrasound From Explosions, *Journal of Geophysical Research: Atmospheres*, **128**(13), e2023JD038725, *reprint*: <https://onlinelibrary.wiley.com/doi/pdf/10.1029/2023JD038725>.

Waxler, R. & Assink, J., 2019. Propagation Modeling Through Realistic Atmosphere and Benchmarking, in *Infrasound Monitoring for Atmospheric Studies: Challenges in Middle Atmosphere Dynamics and Societal Benefits*, p. 509–549, eds Le Pichon, A., Blanc, E., & Hauchecorne, A., Springer International Publishing, Cham.

This paper has been produced using the Blackwell Scientific Publications GJI L^AT_EX2e class file.